# INFORMATION TO USERS

This manuscript has been reproduced from the microfilm master. UMI films the text directly from the original or copy submitted. Thus, some thesis and dissertation copies are in typewriter face, while others may be from any type of computer printer.

**The quality of this reproduction is dependent upon the quality of the copy submitted.** Broken or indistinct print, colored or poor quality illustrations and photographs, print bleedthrough, substandard margins, and improper alignment can adversely affect reproduction.

In the unlikely event that the author did not send UMI a complete manuscript and there are missing pages, these will be noted. Also, if unauthorized copyright material had to be removed, a note will indicate the deletion.

Oversize materials (e.g., maps, drawings, charts) are reproduced by sectioning the original, beginning at the upper left-hand corner and continuing from left to right in equal sections with small overlaps. Each original is also photographed in one exposure and is included in reduced form at the back of the book.

Photographs included in the original manuscript have been reproduced xerographically in this copy. Higher quality 6" x 9" black and white photographic prints are available for any photographs or illustrations appearing in this copy for an additional charge. Contact UMI directly to order.

**UMI**

A Bell & Howell Information Company
300 North Zeeb Road, Ann Arbor MI 48106-1346 USA
313/761-4700 800/521-0600

# A DCT MULTIRESOLUTION ANALYSIS FOR IMAGE DECOMPOSITION AND TEXTURE SEGMENTATION

by

ROLSTON JEREMIAH

A dissertation submitted to the Graduate Faculty in Engineering in partial fulfillment of the requirements for the degree of Doctor of Philosophy

The City University of New York

1998

This manuscript has been read and accepted for the Graduate Faculty in Engineering in satisfaction of the dissertation requirement for the degree of Doctor of Philosophy.

9/17/98
Date

Chair of Engineering Committee

Sept. 17, 1998
Date

Executive Officer

PROFESSOR SAMIR AHMED

PROFESSOR MITRA BASU

PROFESSOR HAISHAN WU

PROFESSOR LEONID ROYTMAN

Supervisory Committee

THE CITY UNIVERSITY OF NEW YORK

# ABSTRACT


## A DCT MULTIRESOLUTION ANALYSIS FOR IMAGE DECOMPOSITION AND TEXTURE SEGMENTATION

by

Rolston Jeremiah

Advisor: Professor Joseph Barba

Variants of the discrete cosine transforms have been used for interpolation and extrapolation in applied mathematics and for data compression and image analysis/synthesis in digital signal processing (DSP). Recent years have seen a revival of interest in using DCT transforms for designing hierarchical interpolation wavelets bases.

This thesis proposes novel approaches to solving the problems associated with texture segmentation and image decomposition using interpolation wavelets having Chebyshev polynomial as basis functions. A new image model called the Generalized Discrete Cosine Transform Wavelet Model (GDCTWM) is presented. Compared with traditional multiresolution methods based on 2-channel filter banks, the pro-

posed model offers the following advantages for dealing with image decomposition and texture segmentation:

1. MRA is carried out using fast DCT algorithms
2. The number of basis functions used equals MAX(N,M), where the image size is $N \times M$ and MAX(N,M) is the maximum of N and M
3. A large class of signals can be compressed to near theoretical optimum ratios since DCTs are used exclusively

The existence of fast DCT algorithms makes practical real time implementation of GDCTWM applications feasible. Moreover, unlike 2-channel filter where the basis functions are scale-shifted copies of a single scaling function, the GDCTWM has a number of basis functions depending upon the dimension of the analyzed signal. The GDCTWM has been shown to possess better energy compaction properties than the class of Daubechies' filters widely used for image decomposition.

# ACKNOWLEDGEMENTS

I wish to acknowledge my mentor Professor Joseph Barba for his guidance and time over the last several years. I admire your kindness and devotion to the undergraduate community here at City College . Special thanks to the CASI group for its support, especially Sandra and Dr. Mars. I also wish to say thanks to all members of the examining committee: Professor Samir Ahmed, Professor Mitra Basu, Professor Haishan Wu and Professor Leonid Roytman.

The research was supported under a grant from the National Science Foundation.

This thesis is dedicated to my decease mother and father, Azonnetta and Mannassah Jeremiah.

# Contents

# List of Tables

# List of Figures

# Chapter 1

## INTRODUCTION

## 1.1 Overview

The aim of this dessertation is to provide a new computational paradigm for image representation and analysis but with the main emphasis on overcoming some of the limitations of current models being used for texture representation/segmentation. The discrete cosine transform wavelet model (DCTWM) achieves this by providing a multi-wavelet, orthogonal bases for representation of images.

The idea is to represent an image using Chebyshev polynomial wavelets. This assumes that image is zero outside the interval [-1,1]. The image can then be de-

composed and synthesized using variants of the DCT. Fast implimentations of these DCT variants are also developed.

## 1.2 Motivation

The advent of wavelets in applied science as introduced by Mallat[1][2] led to a prolific period of new and profound theoritical results on the subject of multiresolution analysis(MRA), a subband splitting scheme widely used by members of the computer vision community[3] [4][5]. Besides putting MRA on solid mathematical foundation, one of the immediate consequences of wavelet theory is that researchers quickly realized that this new computational paradigm could be applied to diverse areas, such as image processing[6], data compression [7] -[16], texture classification/segmentation[17][18] and, more recently, digital communication[19][20]. This work deals with an application of the theory to texture segmentation.

Before wavelets many texture segmentation algorithms were based on computationally intensive statistical methods[21][22]. A problem inherent in these methods is that the probability distributions of the texture elements considered are not usually known a priori and must be estimated from the data. For this reason practical impli-

mentation of optimal estimation algorithms is not usually feasible and semi-optimal algorithms are often used instead. Seeking to reduce the computational burden. some researchers have investigated joint spatial/spatial-frequency(JSSF) approaches. such as the Gaborian representation[23][24][25]. and wavelet based joint spatial/spatial-scale(JSSS) representation[26][27]. in methods which have been suggested to closely parallel the texture discremination scheme of the human visual system(HVS). Researh into HVS indicates that receptive fields of retinal and cortical cells are confined in both their spatial and spatial-frequency bandwidth. That the duality of spatial/spatial-frequency(SSF) representation plays a central role in biological visual systems has been supported by several findings[28][29] New evidence supportive of the theory of JSSF processing of visual information by HVS continue to emerge [4] [30]. In view of the mounting evidence supporting JSSF processing by HVS. many investigators have suggested artificial models which permit a JSSF or JSSS representation. These include the Short-Time Fourier Transform(STFT)[31]. Wavelet Transform(WT), Wigner Distribution(WD)[32][33]. Choi-Willaims Distribution(CWD)[34] [35], and the Ambiguity Function(AF)[36]. The two most prominent represenations are the Gaborian and wavelet based representations.

This work presents a new DCT wavelet based model (DCTWM)[37][38] for texture represenation. The DCTWM also permits a JSSS represenation but has the advan-

tages of being a multi-wavelet representation and of being finite dimensional. We shall call a signal represented by a DCTWM model a ***DCTWM signal***. An orthogonal decomposition of a DCTWM signal can be done efficiently using fast DCT transforms to be introduced in chapter 3. Traditionally, in texture segmentation application, symmetric wavelets are preferred. This preferrence has emerged out of the common practice of classifying pixels by processing blocks of information. A DCTWM model, because of its multi-wavelet status, is able to represent even and odd texture features equally well. Block sizes of the form $2^j + a \times 2^\rho + b$ where $(j, \rho) \in \mathbf{N}$ and $(a, b) \in \{0, 1\}$ are supported under a DCTWM model.

## 1.3 Dissertation Outline

The previous section elucidate the objective of this work. Chapter 2 focuses on some theoritical preliminaries. There, the continuous and discrete wavelet transforms, multirate filtering, and FIR filter banks are reviewed. The GDCTWM model is introduced formally in this chapter. In the main chapter, chapter 3, the focus is on polynomials wavelets on the interval [-1 . 1]. The main theorem on which the decomposition of a GDCTWM signal is based is proven in this chapter. Chapter 4 concerns the application of the DCTWM signal model to multiscale filtering. Chapter

5 deals with the texture segmentation application. A summmary and remarks on future research issues are contained in chapter 6.

# Chapter 2

## Mathematical Preliminaries

The notations and technical background required throughout are discussed in this chapter. Elements of ***Hilbert space*** theory are introduced to deal with continuous transforms, specifically, the ***Short-time Fourier Transform*** (STFT), and ***Wavelet Transform*** (WT). The discretization of anolog signals is at the core of the digital signal processing revolution. It is well known that a band-limited signal can be represented by a set of discrete regular-spaced samples taken in accordance with the nyquist criteria. Contemporary digital signal processing also considers the irregular sampling case and tries to formulate theoritical answers to the issue of representation and reconstructibility from samples obtained via a generalized sampling scheme. Elements of ***frame*** *Theory* are introduced to deal with issues connected to

generalized sampling methods and the discretization of STFT and WT. The discrete wavelet transforms(DWT), and filter banks are described briefly. But first some notations are established.

## 2.1 Notations

The notations used throughout this thesis are presented next. The set of real numbers is denoted $\mathbb{R}$ and the set of complex numbers is denoted by $\mathbb{C}$. The complex conjugate of $z \in \mathbb{C}$ is denoted $\bar{z}$. The set $I \subset \mathbb{R}$ is given by $I = \{x : x \in [-1, 1]\}$. The set of all integers is denoted $\mathbb{Z}$. The subset $\mathbb{N} \subset \mathbb{Z}$ consists of whole numbers $\{0, 1, 2, \cdots\cdots\}$ and the set $\mathbb{N}^+$ consists of the counting numbers $\{1, 2, \cdots\cdots\}$. The Kronecker delta function $\delta_{m,n}$ is defined as

$$\delta_{m,n} = \begin{cases} 1 & m = n \\ 0 & otherwise. \end{cases} \tag{2.1}$$

### 2.1.1 Definitions

The remainder of this section introduces the vector spaces, operators and terminologies encountered in the pending chapters. Throughout we will assume that

$\forall j \in \mathbf{N}$, $V_j \subset L^2_\omega(I)(L^2_\Omega(I^2))$ constitutes a multiresolution of $L^2_\omega(I)(L^2_\Omega(I^2))$. Which Hilbert space is actually meant will be made clear from the context. A few important definitions and operators are defined below.

**Definition 2.1.1** *The Lesbesque space* $L^2(\mathbb{R})$ *is given by*

$$L^2(\mathbb{R}) = \{f : \|f\|^2 = \int_{\mathbb{R}} |f|^2 dx < \infty\}. \tag{2.2}$$

**Definition 2.1.2** *The Hilbert space* $L^2_\omega(I)$ *consists of functions (f,g) satisfying*

$$\langle f, g\rangle_I = \int_I \omega f\, \bar{g}\, dx < \infty \tag{2.3}$$

**Definition 2.1.3** *The Hilbert space* $L^2_\Omega(I^2)$ *consists of functions (f,g) satisfying*

$$\langle f, g\rangle_{I^2} = \int_{I^2} \Omega f\, \bar{g}\, dx\, dy < \infty \tag{2.4}$$

**Definition 2.1.4** *The set C(I) consists of all continuous function* $f : I \to \mathbb{R}$.

**Definition 2.1.5** *The set* $C(I^2)$ *consists of all continuous bidimensional function* $f : I^2 \to \mathbb{R}$.

**Definition 2.1.6** *Let $f \in L^2_\omega(I)$ and $g \in L^2_\Omega(I^2)$. The Chebyshev's series coefficients of $f$ and $g$ are defined by*

$$a_n[f] = 2\langle f, \mathcal{T}_n\rangle_I \tag{2.5}$$

$$a_{mn}[g] = 4\langle g, \mathcal{T}_{mn}\rangle_{I^2} \tag{2.6}$$

Chebyshev polynomials will play an important role in subsequent developments. Let $\mathcal{T}_n$ denotes the $n^{th}$ Chebyshev polynomial. The Hilbert space $L^2_\omega(I)$ is spanned by $\{\mathcal{T}_n\}_{n=0}^{\infty}$. A bidimensional separable Chebyshev polynomial is denoted by $\mathcal{T}_{mn}$ and the Hilbert space $L^2_\Omega(I^2)$ is spanned by $\{\mathcal{T}_{mn}\}_{m,n=0}^{\infty}$.

### 2.1.2 OPERATORS

A subspace $V_j$ is said to be shift invariant if $\forall f \in V_j$ it also holds that $\sigma_{j,\ell} f \in V_j m$. where $\sigma_{j,\ell}$ is a shift operator which maps $V_j$ into itself. The shift and interpolation operators defined below will play prominent roles in the formulation of a multiresolution of $L^2_\omega(I)(L^2_\Omega(I^2))$.

**Definition 2.1.7** *Let $f \in V_j$, a linear subspace of $L^2_\omega(I)$. The shift operator $\sigma_{j,k}$ : $V_j \to V_j$ is given by*

$$(\sigma_{j,\ell} f)(x) = \frac{1}{2} f(x h_{j,k} - \omega(x)\omega(h_{j,k})) + \frac{1}{2} f(x h_{j,k} + \omega(x)\omega(h_{j,k})) \quad x \in I \quad (2.7)$$

where

$$h_{j,k} = cos(\frac{k\pi}{2^j}) \quad (2.8)$$

**Definition 2.1.8** *The interpolation operator $p_j : C(I) \to V_j$ is given by*

$$(p_j f)(x) = \sum_{k=0}^{2^j} \epsilon_{j,k} f(h_{j,k}) \sigma_{j,k}\, \varphi(x) \quad (2.9)$$

**Definition 2.1.9** *The interpolation operator $P_j : C(I^2) \to V_j$ is given by*

$$(P_j f)(x, y) = \sum_{\ell=0}^{2^\ell} \sum_{k=0}^{2^j} \epsilon_{j,k,j,\ell} f(h_{j,k}, h_{j,\ell}) \sigma_{j,k,j,\ell}\, \varphi_j(x, y) \quad (2.10)$$

**Definition 2.1.10** *The Hilbert space $\ell^2(\mathbb{Z})$ is defined as*

$$\ell^2(\mathbb{Z}) = \{X = [x_1, x_2, \ldots] : \|X\|^2 = \sum_{n \in \mathbb{N}} |x_n|^2 < \infty\} \quad (2.11)$$

**Definition 2.1.11** *The finite dimensional Hilbert space $E^m$ is defined as*

$$E^m = \{X = [x_1, x_2, \ldots, x_m] : \|X\|^2 = \sum_{n=1}^{m} |x_n|^2 < \infty\} \quad (2.12)$$

**Definition 2.1.12** *The Fourier transform of* $f \in \{L^2(\mathbb{R}) \bigcap L^1(\mathbb{R})\}$ *is denoted as* $\hat{f}$ *and defined by*

$$\mathcal{F}f(\xi) = \int_{\mathbb{R}} f(t)e^{i\xi t}dt. \tag{2.13}$$

**Definition 2.1.13** *The inverse Fourier Transform of* $f$ *exist and is defined by*

$$\mathcal{F}^{-1}\hat{f}(t) = \frac{1}{2\pi}\int_{\mathbb{R}} f(\xi)e^{-i\xi t}d\xi \tag{2.14}$$

**Definition 2.1.14** *For* $h_n \in \ell^2(\mathbb{Z})$ *the discrete Fourier transform is given by*

$$H(\omega) = \sum_{n\in\mathbb{Z}} h(n)\, e^{in\omega} \tag{2.15}$$

**Definition 2.1.15** *The inverse discrete Fourier transform of* $H(\omega)$ *is given by the inversion formula*

$$h(n) = \frac{1}{2\pi}\int_0^{2\pi} H(\omega)e^{-in\omega}d\omega \tag{2.16}$$

The Z-transform H(z) of $h_n$ is obtained from $H(\omega)$ by setting $z = e^{i\omega}$ in (2.15).

## 2.2 DCTWM Model

The novel signal model introduced in this thesis is called the discrete cosine transform wavelets model(DCTWM). A DCTWM signal $f_j$ can be decomposed into a hierarchical pyramid of lower resolution signals $f_{j-1}$, $f_{j-2}\ldots$ using variants of the DCT. Let $f \in C(I^2)$ and suppose $f_j(k,\ell) \in E^{2^{j+1}}(\mathbb{R}^2)$ are the projection coefficients of $P_j : C(I^2) \rightarrow V_{jm}$. Then, the DCTWM signal $f$ is defined as

$$f_j(x,y) = \sum_{k,\ell=0}^{2^j} \epsilon_{j,k,j,\ell} f_j(k,\ell)\, \sigma_{j,k,j,\ell} \Phi_{j+1}. \tag{2.17}$$

The subspaces $V_j$ are assumed to form a multiresolution of $L^2_\Omega(I^2)$. Details are delayed until chapter 3.

## 2.3 GDCTWM Model

The generalized DCTWM(GDCTWM) is a simple extension to DCTWM which can be derived starting with the assumption that the operator $P_j$ is separable. Assumption holding, we have for $f \in L^2_\Omega(I^2)$

$$(GDCTWM_{j,\rho} f)(x,y) = \sum_{\ell=0}^{2^\rho} \sum_{k=0}^{2^j} \epsilon_{j,k,\rho,\ell}\, f_{j,\rho}(h_{j,k}, h_{\rho,\ell}) \sigma_{j,k,\rho,\ell} \Phi_{j,\rho} \tag{2.18}$$

With this model it is possible to analyze signals of dimension $2^J + 1 \times 2^\rho + 1$. See chapter 3 for more details.

## 2.4 Short-Time Fourier Transform

It has long been known by scientists and mathematicians that the Fourier transform $\hat{f}$ gives only poor information about the local spectral content of f. particular in cases when f is non-stationary. One remedy is to pre-multiply the signal to be analyzed with a window function $\upsilon$, as in $f\,\upsilon(t-\eta)$, prior to taking the Fourier transform. Ideally, the window function should be confined in both its spatial and spatial-frequency extent. If $\upsilon$ is concentrated about $t = 0$, then $\mathcal{F}(f\upsilon(t-\eta))$ can be interpreted as capturing the localized spectral content of f in the vicinity of time $t = \eta$. We called $\mathcal{F}(f\upsilon(t-n))$ the *Short-Time Fourier transform*$(STFT_\upsilon f)$ of $f$ with respect to the window function $\upsilon$ and as such it is given by

$$STFT_\upsilon f(\eta,\xi) = \int_{\mathbb{R}} e^{i\xi t} f(t)\,\overline{\upsilon}(t-\eta)\,dt \tag{2.19}$$

The decay property of $STFT_\upsilon f$ depends on both $f$ and $\upsilon$, as can be seen through the relation $STFT_\upsilon f(\xi,\eta) = e^{-i\eta\xi}\overline{STFT_{\upsilon f}(-\eta,-\xi)}$. As a consequence, the classical dilemma of obtaining good time-frequency localization still requires that $\upsilon$ be

smooth( affects the decay rate and localization properties of $STFT_{\psi}f$) which on the contrary requires a large support of $\psi$ thus destroying the localization of $STFT_{\psi}f$. Designing good window functions remains a central problem in time-frequency analysis.

Recovering $f$ from $STFT_{\psi}f$ is not always possible. inversion of depending on the choice of Gabor wavelets. The following lemma specifies under what condition recovery is possible.

**Lemma 2.4.1** $\forall(\psi, f, g) \in L^2(\mathbb{R})$, *and some finite* $K \in \mathbb{R}$ $f$ *can be recovered from its Short-Time Fourier transform* $STFT_{\psi}f(\xi, \eta)$ *via*

$$f(t) = K \int_{\mathbb{R}^2} e^{\imath\xi\eta(t-x)} STFT_{\psi}f(\xi, \eta) g(t-x) d\xi d\eta \tag{2.20}$$

That is, given $(\psi, f) \in L^2(\mathbb{R})$ and $STFT_{\psi}f$, there exist $g \in L^2(\mathbb{R})$ and $K \in \mathbb{R}$ such that f is given by (2.20).

## 2.5 Continuous Wavelet Transform

The Wavelet transform is a special case of STFT with certain constrains placed on the window function. Let $\psi$ be a window function with properties,

$$0 = \int_{\mathbb{R}} \psi(t)dt \tag{2.21}$$

$$C_\psi = \int_{\mathbb{R}} \frac{|\hat{\psi}(\xi)|^2}{\xi} < \infty \tag{2.22}$$

then $\psi$ is called a wavelet. Define $\psi_{s,\eta}(t) = |s|^{-\frac{1}{2}}\psi\left(\frac{t-\eta}{s}\right)$ $(s,\eta) \in \mathbb{R}$. Then the continuous wavelet transform of $f$ with respect to $\psi$ is given by $(W_\psi f)$

$$\begin{aligned}(W_\psi f)(\eta,\xi) &= |\eta|^{-\frac{1}{2}} \int_{\mathbb{R}} f(t)\overline{\psi}(\frac{t-\xi}{\eta})dt \\ &= \langle f, \psi_{\eta,\xi}\rangle \end{aligned} \tag{2.23}$$

Since $W_\psi f$ is a STFT, the result in lemma 2.4.1 is applicable. Thus, f can be recovered from $W_\psi f$ via

$$f = \frac{1}{C_\psi} \int_{\mathbb{R}^2} W_\psi f(\eta,\xi)\psi(\frac{t-\xi}{\eta})\frac{d\eta d\xi}{\eta^2} \tag{2.24}$$

By the relationship $|\mathcal{F}W_\psi f(\xi,\eta)| = |\eta|^{\frac{1}{2}} \left|\hat{f}\,\hat{\psi}_{\eta\xi}\right|$, it follows that if $\psi(\xi)$ is bandlimited to $[-\Omega,\Omega]$ then $supp\, W_\psi f \subseteq [-\frac{\Omega}{\eta},\frac{\Omega}{\eta}]$. Hence, the choice of the scale parameter $\eta$ determines the localization property of $W_\psi f$. For a given $\psi$ and fixed scale $\eta$, $W_\psi f$ represents the information in f centered around $t = \xi$ at scale resolution $\eta$. To

analyze the portion of f centered about time $t = \xi_1$ at scale $\eta_1$ we simply evaluate $W_\psi f(\eta_1, \xi_1)$. Just how localized is $W_\psi f(\eta_1, \xi_1)$ depends on $\psi$. To put a quantitative measure on the notion of time-frequency(scale) localization define

$$t_{avg} = \frac{1}{\|\psi\|^2} \int_{\mathbb{R}} t \, |\psi(t)|^2 \, dt \tag{2.25}$$

$$t_{var} = \frac{1}{\|\psi\|} \int_{\mathbb{R}} (t - t_{avg})^2 \, |\psi(t)|^2 \, dt \tag{2.26}$$

Similar expressions for $\eta_{avg}$ and $\eta_{var}$ are obtained from (2.25) and (2.26) by replacing $\psi$ with $\hat{\psi}(\xi)$ in both cases. A spatial domain window centered at $t_{avg}$ has effective width $2t_{var}$ and is defined over the interval $[t_{avg} - t_{var}, t_{avg} + t_{var}]$. The spatial-scale window is defined over the interval $[\xi_{avg} - \xi_{var}, \xi_{avg} + \xi_{var}]$. These two one dimensional windows form a rectangular region of effective area $4\eta_{var}t_{var}$ over the TF-plane. This is shown in figure 2.8. It is usually desirous in time-scale analysis to employ an analyzing function having a small effective area in the TF-plane. However, the minimum effective area is governed by the *Uncertainty Principle*

$$t_{var}\xi_{var} \geq \frac{1}{2\pi}, \tag{2.27}$$

equality holding only for the Guassian window.

## 2.6 Multiresolution of $L^2(\mathbb{R})$

Let $V_j$ be a subspace of $L^2(\mathbb{R})$ span by $\phi_{j,k}$ that is $V_j = span\{\phi_{j,k}\}_{j\in\mathbb{Z}}$, where $\phi_{j,k} = \phi(2^j - k)$. We will say that the sequence of nested subspaces $\{V_j\}_{j\in\mathbb{Z}}$ constitutes a multiresolution of $L^2(\mathbb{R})$ if the following conditions are met:

1. $\ldots V_1 \subset V_0 \subset V_1 \ldots$

2. $V_j = V_{j+1} \oplus W_{j+1}$

3. $L^2(\mathbb{R}) = \{\bigcup V_j\}_{j\in\mathbb{Z}}$

4. $g(x) \in V_j \longrightarrow g(x-n) \in V_j$

5. $g(x) \in V_j \longrightarrow g(2x) \in V_{j+1}$

6. $\exists \in V_0\, \phi$ such that $\phi_{0,n}$ is an orthonormal basis for $V_0$

It has been shown that certain sampling schemes applied to the mother wavelets give rise to discrete wavelet frames. If the wavelet family

$$\psi_{j,m}(x) = 2^{-j/2}\psi(2^{-j}x - m) \tag{2.28}$$

is a frame in $L^2(\mathbb{R})$ and the above criteria are satisfied. $\psi$ is said to be derivable from a multiresolution analysis. However, not all wavelets can be derived starting with a multiresolution paradigm. But under the above conditions and the frame condition on (2.28), there exist sequences $g_n$ and $h_n$ such that

$$\phi(t) = \sum_{n\in\mathbb{Z}} h_n \phi(2t - n) \tag{2.29}$$

$$\psi(t) = \sum_{n\in\mathbb{Z}} g_n \phi(2t - n)a \tag{2.30}$$

Since the wavelet family $\{\psi_{j,k}\}$ is frame in $L^2(\mathbb{R})$ then results from frame theory guarantee the existence of a dual wavelet $\tilde{\psi}$ and scaling function $\tilde{\phi}$ satisfying (2.29-2.30) with $\tilde{h}_n$ and $\tilde{g}_n$ replacing $h_n$ and $g_n$ respectively. In order that $V_j \perp W_j$ and perfect reconstruction be possible it is necessary that the sequences (filters) $g_j$ and $h_n$ satisfy the modulation domain relations

$$H(z)\tilde{H}(z) + G(z)\tilde{G}(z) \quad = 1 \tag{2.31}$$

$$H(-z)\tilde{H}(z) + G(-z)\tilde{G}(z) = 0 \tag{2.32}$$

In most application it common to take $g_n = (-1)^n \tilde{h}(1-n)$ and $\tilde{g}(n) = (-1)^n h(1-n)$ with $\tilde{h}(n) = h(-n)$. These choices reduce the design problem to one of finding a filter

$h_n$ satisfying $|H(\omega)|^2+|H(\omega+\pi)|^2 = 1$. The discrete wavelet transform of a sequence $f_n$ is carried out using the high-pass filters $\bar{g}_n$ and $g_n$ and the low-pass filters $h_n$ and $\bar{h}_n$. A two channel filter bank implementation is shown in figure 2.8. The reader is referred to references [[16]-citech:osri] for possible design alternatives of $h_n$.

## 2.7 Frame Theory

In actual implementation of signal processing algorithms it is necessary to sample in some way the signal or some transformation of the signal in order that the underlying objective be amendable to numerical methods. Clearly, depending on the signal's vector space topology, the sampling scheme adapted must be consistent with proven methods allowing for signal recovery from the available samples. Today a great deal of attention is given to generalized sampling as oppose to uniform sampling. In the case of uniform sampling it is well known that a band-limited signal $f \in L^2(\mathbb{R})$ with $supp\, \hat{f} = [-\Omega, \Omega]$ is uniquely represented by samples taken at or above the nyquist rate $\frac{\Omega}{2} \leq T$. Reconstruction in that instance is by $f(t) = \sum_{n\in\mathbb{Z}} f(nT)\frac{sin(\Omega t - nT)}{t\Omega}$. Often is the transform domain representation which must be sampled, thus samples are taking over the time-frequency(TF) plane. A study of signal representation via generalized samples requires the introduction of the concept of a ***frame.*** In

general it is known that a signal can be reconstructed from sample values taken over a sufficiently dense discrete set of points in the TF-plane. More specifically, the density of sample points is related to the bandwidth of the analyzed signal.

**Definition 2.7.1** *A sequence* $\{g_\jmath,\ \jmath \in \mathbb{Z}\}$ *is called a* ***tight frame*** *for Hilbert space* $L^2(\mathbb{R})$ *if* $\forall f \in L^2(\mathbb{R})$ *it holds that*

$$\|f\|_2 = \left(\sum_{\jmath\in\mathbb{Z}} |\langle f, g_\jmath\rangle|^2\right)^{1/2} \tag{2.33}$$

As a direct consequence to definition 2.7.1 $f = Sf = \sum_{\jmath\in\mathbb{Z}} \langle f, g_\jmath\rangle\, g_\jmath$, whenever the sequence $\{g_\jmath\}_{\jmath\in\mathbb{Z}}$ constitute a tight frame for $L^2(\mathbb{R})$. In mathematical literature S is called the frame operator. Despite this orthonormal-like representation, a frame is not in general a basis for $L^2(\mathbb{R})$ and one is free to impose practical constrains on the coefficients $\langle f, g_\jmath\rangle$ in the expansion. The coefficients, however, contain all the information present in the signal and in the special case when $\{g_\jmath\}$ is a tight ***affine frame***, meaning that all members of the family are derivable from a single prototype $g$ by translation and scaling(dilation), these coefficients permits the identification of region in the signal which match strongly with a scaled version of the prototype. An example of a affine frame would be $\psi_{s,\eta}$, subject to the constraints imposed on $\psi$ . Affine frames are special cases of the class of ***coherent frames***, frames generated by some group action on a single prototype. The general definition of a frame is

offered below.

**Definition 2.7.2** *The sequence* $\{g_j, j \in \mathbb{Z}\}$ *is a frame in the Hilbert space* $L^2(\mathbb{R})$ *if* $\forall f \in L^2(\mathbb{R})$ *there exist constants* $A$ *and* $B$ *with* $0 < A \leq B$ *such that*

$$A\|f\|^2 \leq \left(\sum_{j\in\mathbb{Z}} |\langle f, g_j\rangle|^2\right)^{1/2} \leq B\|f\|^2 \tag{2.34}$$

A frame is a tight frame when the frame bounds A and B are equal. The existence of the lower bound $A > 0$ ensures that the signal can be reconstructed from the coefficients as $f = \sum_{j\in\mathbb{Z}} \langle f, g_j\rangle \tilde{g}_j$, with $\tilde{g}_j$ being the dual frame relative to $g_j$. The dual frame is given by $\tilde{g}_j = S^{-1}g_j$. Note that unless A=B, $f \neq Sf$ and in such general cases reconstruction is usually carried out using iterative algorithms. One such algorithm is the so-called ***frame algorithm***, directly derivable in terms of the frame operator S. The algorithm proceeds as follows:

**Frame Algorithm**

$$\text{set } f^{(0)} = \nu S f \tag{2.35}$$

$$f^{(n+1)} = f^{(n)} + \nu S\left(f - f^{(n)}\right) \tag{2.36}$$

The rate of convergence depends on the choice of $\nu$. Convergence or divergence may occur, depending on whether $\nu$ is too small or too large. It has been proven that the

optimal choice is $\nu = \frac{2}{A+B}$. Unfortunately, it is usually quite difficult to estimate the frame bounds. This has served as the impetus to develop new adaptive algorithms that estimate the frame bounds during the iterative cycle. In fact, some well known algorithms have been adapted to replace the frame algorithm. These include the ***steepest descent***(SD), ***conjugate gradient***(CG) and the ***projection onto convex sets***(POCS) algorithms. The frame algorithm itself has been modified in some instances giving rise to the class of *accelerated frame algorithms.*

As mentioned above it is possible, albeit difficult at times, to recover a signal from its frame-representation. Sf. Therefore it is reasonable to inquire what sampling scheme applied to wavelet transform(STFT) give rise to wavelets frames( STFT frames). This is important, since then the dual wavelet exists thus allowing reconstruction. The answer in the case of the wavelet transform is given below in the form of theorem proved elsewhere.

**Theorem 2.7.1** *Let* $f \in L^1(\mathbb{R}) \bigcup L^2(\mathbb{R})$ *be band-limited with* $supp\, \hat{f} = [-\Omega, -\xi] \bigcup [\xi, \Omega]$ *and* $\hat{f}(\eta) \neq 0$ *for* $\sqrt{\frac{\xi\Omega}{\lambda}} < |\eta| < \sqrt{\xi\Omega\lambda}$ *for some* $\lambda$ *satisfying* $1 < \lambda < \frac{\Omega}{\xi}$. *If* $(s_j)_{j\in\mathbf{Z}}$ *and* $(x_{j,\kappa})_{j,\kappa} \in \mathbb{Z}$ *are admissible sequences satisfying*

$$\sup_{j\in\mathbf{Z}} \frac{s_{j+1}}{s_j} \leq \lambda < \frac{\Omega}{\xi} \tag{2.37}$$

$$\delta := \sup_{j,\kappa\in\mathbf{Z}} \frac{x_{j,\kappa+1} - x_{j,\kappa}}{s_j} < \frac{\pi}{\Omega} \tag{2.38}$$

$$\rho := \sum_{j\in\mathbb{Z}} 0.5\, ln\frac{s_{j+1}}{s_{j-1}} |f(s_j, \eta)|^2 \tag{2.39}$$

*and with the constants* $a = inf_{\eta\in\mathbb{R}}\rho$ *and* $b = sup_{\eta\in\mathbb{R}}\rho$ *both greater than zero. then*

$$\begin{aligned} a\left(1-\frac{\delta\Omega}{\pi}\right)^2 \|f\|^2 &\leq \sum_{j,\kappa\in\mathbb{Z}} \frac{1}{4}(x_{j,\kappa+1} - x_{j,\kappa})\, ln\left(\frac{s_{j+1}}{s_{j-1}}\right) \\ |W_\psi f(x_{j,\kappa}, s_j)| &\leq b\left(1+\frac{\delta\Omega}{\pi}\right)^2 \|f\|^2 \end{aligned} \tag{2.40}$$

*Under the above condition* $f$ *is uniquely determined by the generalized samples of its wavelet transform in(2.40).*

## 2.8 Discrete Wavelet Transform

Let $f \in L^2(\mathbb{R})$ and suppose that the projection of $f$ onto the subspace $V_j$ is given as

$$f_j = P_{V_j} f(x) = \sum_{k\in\mathbb{Z}} C_k^j\, \phi(2^{-j}x - k). \tag{2.41}$$

For a coarser resolution representation of $f$ coefficients $C_k^{j+1}$ and $D_k^{j+1}$ are required such that $f_j = f_{j+1} + \lambda_{j+1}$ and

$$f_{j+1} = P_{V_{j+1}} f(x) = \sum_{k\in\mathbb{Z}} C_k^{j+1}\, \phi(2^{-(j+1)}x - k) \tag{2.42}$$

$$\lambda_{j+1} = P_{W_{j+1}} f(x) = \sum_{k\in\mathbb{Z}} D_k^{j+1}\, \psi(2^{-(j+1)}x - k) \tag{2.43}$$

Here, $P_{V_{j+1}} f$ represents a coarser resolution version of $f_j$ and $P_{W_{j+1}} f$ contains the details $f_j - f_{j+1}$. The discrete wavelet transform is concerned with the efficient computation of $C_k^{j+1}$ and $D_{kJ} + 1$ given $C_k^j$. It can be shown that efficient decomposition formulae are by

$$C_k^{j+1} = (C^j \downarrow 2) \otimes h(k - \cdot) \tag{2.44}$$

$$D_k^{j+1} = (C^j \downarrow 2) \otimes g(k - \cdot) \tag{2.45}$$

The synthesis formulae are given in terms of the dual wavelet and scaling function coefficients.

$$C_k^j = \left(C^{j+1} \uparrow 2\right) \otimes \tilde{h}(k - \cdot) + \left(D^{j+1} \uparrow 2\right) \otimes \tilde{g}(k - \cdot) \tag{2.46}$$

The process can be repeated several levels to obtain lower and lower resolutions. The block diagram of figure 2.8 portrays the two-channel case. More general decomposition schemes in the form of m-channel filter banks are known to exist.

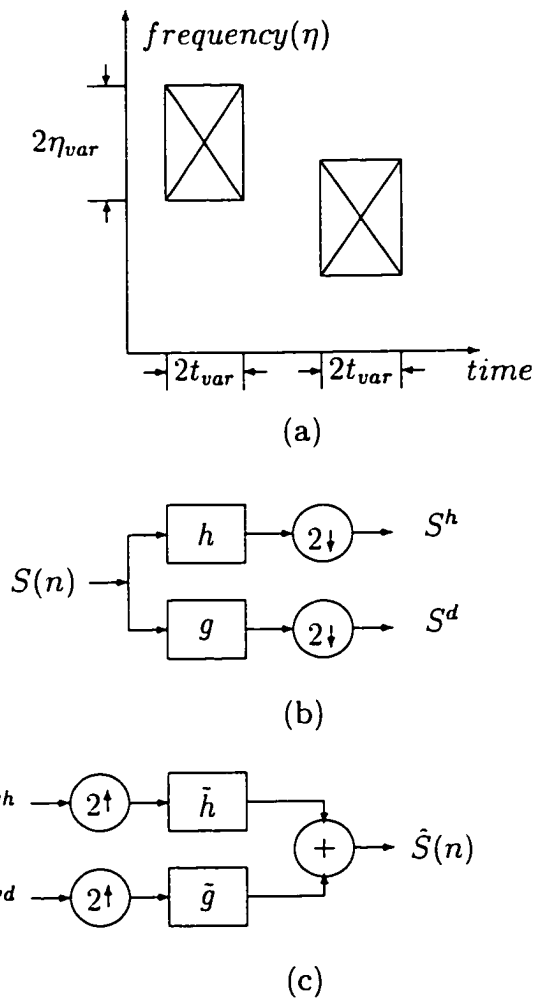


Figure 2.1: (a) Guassian time-frequency window in the TF-plane (b) Analysis 2-channel filter bank (c) Synthesis filter bank for part (b)

# Chapter 3

## Polynomial Wavelets

## Introduction

While most wavelets are designed for $L^2(\mathbb{R})$ real applications always involve signals of finite duration. As a result, particular to the case of multiscale filtering, undesirable edge effects arise naturally in implementations of algorithms developed for $L^2(\mathbb{R})$ being applied to signals in $\mathrm{L}^2(\beta)$, where $supp(\beta)$ is finite. For example, these effects may arise when a signal is synthesized from its lower resolution projections and are due to decimation in the decomposition phase of the application. Since most multirate systems employ decimators in a myriad of applications, it is essential that

there be effective ways of managing this signal processing problem. Methods of handling edge effects were proposed by Gunnar[41], Meyer [42], and more recently Prestin[43] introduced polynomial wavelets on [-1,1]. The method of Gunnar and Vetterli consists of symmetrically extending the signal beyond its natural boundary at either extreme of its support. Meyer examined the restriction of wavelets on the real line to a bounded subset $\mathcal{J} \subset \mathbb{R}$. His construction, however, is ill conditioned for wavelets with large support. A more stable algorithm for wavelets on [0,1] was proposed by Cohen et al[44].

This chapter describes a class of Chebyshev's polynomial wavelets on I and their extension to $I^2$. The multiresolution analysis of $L^2_\Omega(I^2)$characterized by these wavelets is not prone to the kind of edge distortion common in filter bank implementations. Fast decomposition and reconstruction algorithms are also derived. An image processing application is delayed until chapter 4.

## 3.1 Chebyshev Polynomials

The $n^{th}$ Chebyshev polynomial is denoted $\mathcal{T}_n$ and is defined by

$$\mathcal{T}_n(x) = cos(n\, arcos(x)) \quad x \in I, \quad n = 0, 1, \ldots \tag{3.1}$$

These polynomials are known to have many attractive mathematical properties, including orthogonality over the closed interval [-1,1](see 3.2) and rapid convergence rate of expansion coefficients. The recurrence relationship $\mathcal{T}_{n+1} = 2\mathcal{T}_n(x) + x\,\mathcal{T}_{n-1}(x)$ facilitates the computation of $\mathcal{T}_n$ when is large. The property most relevant to subsequent developments is that the set $\{\mathcal{T}_n\}_{n=0}^{\infty}$ constitutes an orthogonal bases for $L^2_\omega(I)$, the Hilbert space of functions $(f, g)$ satisfying the scalar weighted inner product

$$\langle f, g\rangle_I = \frac{1}{\pi}\int_I \omega f\,\bar{g}\,dx \;< \infty \tag{3.2}$$

The orthogonality of Chebyshev polynomials with respect to (3.2) is governed by

$$\langle T_m, \mathcal{T}_n\rangle_I = \begin{cases} 1 & m = n = 0 \\ \frac{1}{2} & m = n \neq 0 \\ 0 & otherwise. \end{cases} \tag{3.3}$$

where in each expression above and throughout this thesis

$$\omega(x) = (1 - x^2)^{-\frac{1}{2}}. \tag{3.4}$$

Trigonometric interpolation has been extensively investigated by many ([45]-[47]) for the purpose of constructing hierarchical bases. Recent developments have lead to the construction of interpolating wavelets for spaces other than $L^2(\mathbb{R})$. Starting with Chebyshev polynomials, Baszenski and Tasche[46] constructed such a basis for

$L^2_\Omega(I^2)$. Their construction relies heavily on the interpolating operator $\sigma_{j\,k}$ defined by

$$\begin{aligned}\sigma_{j,k}f(x) =& \frac{1}{2}f(xh_{j,k} - [\omega(x)\omega(h_{j,k})]^{-\frac{1}{2}}) + \\ & \frac{1}{2}f(xh_{j,k} + [\omega(x)\omega(h_{j,k})]^{-\frac{1}{2}}) \quad f \in C(I).\end{aligned} \tag{3.5}$$

For $f \in C(I)$, the space of continuous functions on I. by $a_n[f]$ we shall mean the $n^{th}$ coefficient of $f$ in its Chebyshev series. The operator $\sigma_{j,k}$ can be shown to have the following properties.

$$\sigma_{j,k}\mathcal{T}_n = cos(\frac{nk\pi}{2^j})\mathcal{T}_n \tag{3.6}$$

$$a_n[\sigma_{j,k}\,f] = cos(\ \frac{nk\pi}{2^j}\ )\,a_n[f] \tag{3.7}$$

The above results will play an important role in the construction of hierarchical bases for the bidimensional space $L^2_\Omega(I^2)$. A review of interpolating polynomials wavelets on $L^2_\omega(I)$ is in order. An extension to $L^2_\Omega(I^2)$ will follow in a later section.

## 3.2 Multiresolution of $L^2_\omega(I)$

The goal of this section is to highlight the roles played by Chebyshev polynomials and two variants of the discrete cosine transform in a multiresolution analysis of $L^2_\omega(I)$. The operator $\sigma_{j,k}$ will serve as an analytical tool. To characterize the MRA

of $L^2_\omega(I)$. let $\phi_j$ be the scaling function and $\psi_{j+1}$ the mother wavelet on level $j$ and define subspaces $V_j$ and $W_j$ of $L^2_\omega(I)$ by

$$V_j = \text{span}\{\sigma_{j,k}\,\phi_j\}_{k=0}^{2^j} \tag{3.8}$$

$$W_j = \text{span}\{\sigma_{j+1,2k+1}\,\psi_{j+1}\}_{k=0}^{2^j-1} \tag{3.9}$$

The objective now is to choose $a_n[\psi_j]$ and $a_n[\phi_{j+1}]$ such that $V_{j+1} = V_j \oplus W_j$. The following choices of expansion coefficients satisfy this requirement.

$$a_n[\phi_j] = 2^{1-j}\begin{cases} 1 & n = 0, \cdots\cdots, 2^j - 1 \\ 0.5 & n = 2^j \\ 0 & \text{otherwise.} \end{cases} \tag{3.10}$$

$$a_n[\psi_{j+1}] = 2^{1-j}\begin{cases} 1 & n = 2^j + 1, \cdots\cdots, 2^{j+1} - 1 \\ 0.5 & n = 2^{j+1}. \\ 0 & \text{otherwise.} \end{cases} \tag{3.11}$$

It is immediately clear from (3.2, 3.3) that $\phi_j \perp \psi_{j+1}$. By (3.5.3.6) we still have $\sigma_{j,k}\phi_j \perp \sigma_{j,2k+1}\psi_{j+1}$ and hence this orthogonality, by extension, applies to subspaces $V_j$ and $W_j$. The graphs in figure 3. 3.1 display the sinusoidal behavior of functions under consideration. To summarize, we have argued that the set $a = \{\mathcal{T}_n\}_{n=0}^{2^j}$ spans $V_j$ and that the set $b = \{\mathcal{T}_n\}_{n=2^j+1}^{2^{j+1}}$ spans $W_j$. Then by definition (3.8), the set $\{a \cup b\}$

spans $V_{j+1}$. Hence, it immediately follows that $V_j \perp W_j$ and that

$$V_{j+1} = V_j \oplus W_j. \tag{3.12}$$

Equation (3.12) establishes the existence of a multiresolution of $L^2_{\omega}(I)$ and of scaling-symbol relationships among $a_n[\phi_j]$, $a_n[\psi_{j+1}]$, and $a_n[\phi_{j+1}]$. Scaling-symbol relations are key players in decomposition and reconstruction algorithms of function spaces. Recall that for $f \in C(I)$, the space of continuous functions on I, the projection operator $p_j : C(I) \to V_j$ is given by

$$p_j f = \sum_{k=0}^{2^j} \epsilon_{j,k} f(\cos(\tfrac{k\pi}{2^j}))\sigma_{j,k}\, \phi_j. \tag{3.13}$$

Since $\phi_j$ and $\psi_{j+1}$ must respectively satisfy $\phi_j = p_{j+1}\, \phi_j$ and $\psi_{j+1} = p_{j+1}\psi_{j+1}$, then

$$\phi_j = \sum_{k=0}^{2^{j+1}} \epsilon_{j+1,k}\, \phi_j(\cos(\tfrac{k\pi}{2^{j+1}}))\sigma_{j+1,k}\, \phi_{j+1} \tag{3.14}$$

and

$$\psi_{j+1} = \sum_{k=0}^{2^{j+1}} \epsilon_{j+1,k}\, \psi_{j+1}(\cos(\tfrac{k\pi}{2^{j+1}}))\sigma_{j+1,2k+1}\, \psi_{j+1}. \tag{3.15}$$

Derivation of actual two-scale relations among the above Chebyshev coefficients is based entirely on the properties of the shift-operator $\sigma_{j,\ell}$, DCT-I and DCT-II transforms, and also on equations(3.13,3.10,3.11). Results were given in [43] without proof. A statement and proof are granted next.

**Lemma 3.2.1** *Let $\Phi_j$ be the scaling function on $V_j$ as defined in3.8 and $\psi_{j+1}$ the wavelet in $W_j$ defined in (3.11). Then*

$$a_n[\varphi_j] = 2\, A_{j+1,n}\, a_n[\varphi_{j+1}] \tag{3.16}$$

$$a_n[\psi_{j+1}] = 2\, B_{j+1,n}\, a_n[\phi_{j+1}], \tag{3.17}$$

*where*

$$A_{j+1,n} = \begin{cases} 1 & n = 0, \cdots, 2^j - 1 \\ 1/2 & n = 2^j \\ 0 & otherwise. \end{cases} \tag{3.18}$$

*and*

$$B_{j+1,n} = \begin{cases} 1 & n = 2^j + 1, \cdots, 2^j - 1 \\ 0 & otherwise. \end{cases} \tag{3.19}$$

(3.20)

# Proof

$$\phi_j = \sum_{k=0}^{2^{j+1}} \epsilon_{j+1,k}\, \phi_j(cos(\frac{m\pi}{2^{j+1}}))\, \sigma_{j+1,k} \phi_{j+1} \tag{3.21}$$

Using the properties of $\sigma_{j,k}$ and substituting for $\phi_j(cos(\frac{k\pi}{2^{j+1}}))$ we now have

$$a_n[\phi_j] = \sum_{p=0}^{2^j} \epsilon_{j,p}\, a_p[\varphi_j] \sum_{k=0}^{2^{j+1}} \epsilon_{j+1,k}\, cos\left(\frac{pk\pi}{2^{j+1}}\right) cos\left(\frac{nk\pi}{2^{j+1}}\right)\, a_n[\phi_{j+1}] \tag{3.22}$$

$$= 2\sum_{p=0}^{2^J} \frac{\epsilon_{J,p}\, a_n[\phi_{J+1}]}{\epsilon_{J+1,p}} COS_{J+1}(n,p) \tag{3.23}$$

where

$$COS_{J+1}(n,p) = 2^{1-(J+1)}\, \epsilon_{J+1,p} \sum_{k=0}^{2^{J+1}} \epsilon_{J+1,k} cos(\frac{kp\pi}{2^{J+1}}) cos(\frac{kn\pi}{2^{J+1}}) \tag{3.24}$$

$$= \delta_{n,p} \tag{3.25}$$

Hence

$$a_n[\phi_J] = 2\sum_{p=0}^{2^J} \frac{\epsilon_{J,p}\, a_n[\phi_{J+1}]}{\epsilon_{J+1,p}} \delta_{n,p} \tag{3.26}$$

$$= 2\frac{\epsilon_{J,n}\, a_p[\phi_{J+1}]}{\epsilon_{J+1,n}} \delta_{n,p} \quad n = 0, \ldots, 2^J \tag{3.27}$$

Define $A_{J+1,n} = \frac{\epsilon_{J,n}}{\epsilon_{J+1,n}}$ and 3.16 follows. Likewise

$$a_n[\psi_{J+1}] = \sum_{p=2^J+1}^{2^{J+1}} a_n[\phi_{J+1}] COS_{J+1}(n,p) \tag{3.28}$$

$$= 2\, a_n[\phi_{J+1}] \delta_{n,p} \quad p = 2^J + 1, \ldots, 2^{J+1} \tag{3.29}$$

Define $B_{J+1,n} = \delta_{n,p}$ where $p = 2^J + 1, \ldots, 2^{J+1}$ and 3.17 follows □

Up to this point the main results concern the existence of MRA of $L^2_{\omega}(I)$(3.12) and the relations(3.16 -3.17). We now go further to describe the decomposition of $V_{J+1}$ into orthogonal components.

Assume $f_{J+1}(k) = f(h_{J+1,k})$ $k \in \{0, \cdots, 2^{J+1} + 1\}$ are samples (see [47]) of some continuous function $f \in C(I)$. When $f$ is expressed as on the right hand side of

(3.13), we shall refer to $f$ as a DCTWM signal and to the model formulation as the DCTWM model, where DCTWM is acronym for discrete cosine transform wavelet model. Let the DCTWM signal $f_{j+1} \in V_{j+1}$ be given by $f_{j+1} = f_j + g_j$, where $f_j \in V_j$ and $g_j \in W_j$. The expansion of $f_{j+1}$ on $V_{j+1}$ can be written as

$$\begin{aligned} f_{j+1} &= \sum_{k=0}^{2^{j+1}} \epsilon_{j+1,k} f_{j+1}(k)[\sigma_{j+1,k}\, \phi_{j+1}] \\ &= \sum_{k=0}^{2^j} \epsilon_{j,k}\, f_j(k)\, [\sigma_{j,k}\, \phi_j] + \sum_{k=0}^{2^j-1} g_j(k)\, [\sigma_{j+1,2k+1}\, \psi_{j+1}] \end{aligned} \tag{3.30}$$

The final term in (3.30) is the expansion of $g_j$ on $W_j$. Taking the $n^{th}$ coefficient on both sides of 3.30 and using property (3.6), we will find after some manipulation that

$$\hat{f}_{j+1}(n)\, a_n[\phi_{j+1}] = \{2A_{j+1,n}\, \hat{f}_j(n) + 2B_{j+1,n}\, \hat{g}_j(n)\}\, a_n[\phi_{j+1}] \tag{3.31}$$

where

$$\hat{f}_{j+1}(n) = \sum_{k=0}^{2^{j+1}} \epsilon_{j+1,k}\, f_{j+1}(k) cos(\frac{nk\pi}{2^{j+1}}) \tag{3.32}$$

$$\tilde{g}_j(n) = \sum_{k=0}^{2^j-1} g_j(k)\, cos(\frac{(2k+1)n\pi}{2^{j+1}}) \tag{3.33}$$

Following established conventions, $\hat{f}_{j+1}$ is called a $(2^{j+1}+1)$-point DCT-I transform of the sequence $f_{j+1}$ and $\tilde{g}$ is called a $(2^j)$-point DCT-II transform of the discrete sequence $g_j$. Further manipulations of (3.31) yields the following important results.

$$\hat{f}_j(n) = \frac{\hat{f}_{j+1}(n)}{2A_{j+1,n}} \quad n = 0, \ldots, 2^j \tag{3.34}$$

$$\tilde{g}_j(n) = \frac{\hat{f}_{j+1}(n)}{2B_{j+1,n}} \quad n = 2^j + 1, \ldots, 2^{j+1}. \tag{3.35}$$

The DCTWM signals $f_j$ and $g_j$ can be recovered from $\hat{f}$ and $\tilde{g}$ by inverse DCT-1 and DCT-2 transforms.

The above shows that we can decomposed $V_{j+1}$ using the DCT-I and DCT-II transforms. This property can readily be extended to $L^2_\Omega(I^2)$, the task we take on in the next section.

## 3.3 Multiresolution of $L^2_\Omega(I^2)$

In this section we extend the multiresolution analysis of the previous section to $L^2_\Omega(I^2)$, the Hilbert space of functions $(f, g)$ satisfying the scalar inner product

$$\langle f, g \rangle_{I^2} = \frac{1}{\pi^2} \int_{I^2} \Omega(x, y)\, f\, \bar{g}\, dx\, dy \tag{3.36}$$

where in the equation above and throughout this thesis

$$\Omega(x, y) = \omega(x)\, \omega(y) \tag{3.37}$$

By $\mathcal{T}_{mn}$ we shall mean a bidimensional Chebyshev polynomial. It now easy to show that

$$L^2_\Omega(I^2) = \text{span}\{\mathcal{T}_{mn}\}_{m,n=0}^{\infty} \tag{3.38}$$

where

$$\mathcal{T}_{mn} = \mathcal{T}_m(x)\,\mathcal{T}_n(y) \tag{3.39}$$

Any DCTWM signal $f \in L^2_\Omega(I^2)$ has an alternative Chebyshev series expansion given by

$$f = \frac{a_{00}[f]}{4} + \sum_{n=1}^{\infty}\left[\frac{a_{0n}[f]}{2}\mathcal{T}_{0n} + \frac{a_{n0}[f]}{2}\mathcal{T}_{n0}\right] + \sum_{m,n=1}^{\infty} a_{mn}\mathcal{T}_{mn} \tag{3.40}$$

where

$$a_{mn}[f] = 4\,\langle f\,\mathcal{T}_{mn}\rangle_{I^2} \tag{3.41}$$

The following definitions will be helpful in the characterization of the multiresolution decomposition of $L^2_\Omega(I^2)$.

**Definition 3.3.1**

$$V_j = span\{\sigma_{j,k,j,\ell}\,\Phi_j\} \tag{3.42}$$

$$W_j^d = span\{\sigma_{j+1,2k+1,j+1,2\ell+1}\,\Psi_{j+1}\} \tag{3.43}$$

$$W_j^h = span\{\sigma_{j,k,j+1,2\ell+1}\,\Psi_{j+1}^h\} \tag{3.44}$$

$$W_j^v = span\{\sigma_{j+1,k,j,\ell}\,\Psi_{j+1}^v\} \tag{3.45}$$

The scaling function in $V_j$ and the wavelets in $W_j^d, W_j^h$ and $W_j^v$ are respectively denoted by $\Phi_j, \Psi_{j+1}^d, \Psi_{j+1}^h$ and $\Psi_{j+1}^v$. Definitions are offered below.

**Definition 3.3.2**

$$\Phi_j = \phi_j(x)\phi_j(y) \tag{3.46}$$

$$\Psi_{j+1} = \psi_{j+1}(x)\psi_{j+1}(y) \tag{3.47}$$

$$\Psi_{j+1}^h = \phi_j(x)\psi_{j+1}(y) \tag{3.48}$$

$$\Psi_{j+1}^v = \psi_j(x)\phi_j(y). \tag{3.49}$$

The bidimensional shift operator is defined via its action on a DCTWM signal. Assuming $\Phi_j \in L_\Omega^2(I^2)$ is such a signal, then take $\sigma_{j,k,\rho,\ell}\,\Phi_j$ to mean

$$\sigma_{j,k,\rho,\ell}\,\Phi_j = \sigma_{j,k}\,\phi_j(x)\,\sigma_{\rho,\ell}\phi_j(y). \tag{3.50}$$

The above interpretation leads to the following lemma.

**Lemma 3.1** *Let $f \in L_\Omega^2(I^2)$ and let $\sigma_{j,k,\rho,\ell}$ be the bidimensional shift operator. We now have*

$$\sigma_{j,k,\rho,\ell}\mathcal{T}_{mn} = cos\left(\frac{mk\pi}{2^j}\right) cos\left(\frac{n\ell\pi}{2^\rho}\right) \tag{3.51}$$

$$a_{mn}[\sigma_{j,k,\rho,\ell}\,f] = cos\left(\frac{mk\pi}{2^j}\right) cos\left(\frac{n\ell\pi}{2^\rho}\right) a_{mn}[f] \tag{3.52}$$

## Proof

By definition $\mathcal{T}_{mn} = \mathcal{T}_m \mathcal{T}_n$, and thus $\sigma_{j,k,\rho,\ell}\mathcal{T}_{mn} = \sigma_{j,k}\mathcal{T}_m(x)\sigma_{\rho,\ell}\mathcal{T}_n(y)$. Equation (3.51) then follows from direct application of (3.6-3.7). Similarly, we also have

$$f = \sum_{m,n=0}^{\infty} a_{mn}[f]\mathcal{T}_{mn} \tag{3.53}$$

$$a_{rs}[\sigma_{j,k,\rho,\ell} f] = \sum_{m,n=0}^{\infty} a_{mn}[f] cos\left(\frac{rk\pi}{2^j}\right) cos\left(\frac{s\ell\pi}{2^\rho}\right) a_{rs}[\mathcal{T}_{mn}] \tag{3.54}$$

$$= \sum_{m,n=0}^{\infty} a_{mn}[f] cos\left(\frac{rk\pi}{2^j}\right) cos\left(\frac{s\ell\pi}{2^\rho}\right) \delta_{r,m}\delta_{s,n} \tag{3.55}$$

and (3.52) follows from the last equation above □.

Two-scale symbol expressions relating $a_n[\phi_j]$ and $a_n[w_{j+1}]$ to $a_n[\phi_{j+1}]$ were derived earlier( lemma 3.2.1). Using (3.46-3.49) as the starting point, the corresponding two-scale symbols on $L^2_\Omega(I^2)$ can be shown to be combination of the product of the two-scale symbols on $L^2_\omega(I)$. These two-scale symbols are required for the decomposition of $V_{j+1}$, a task we take on later. The next theorem provides expressions for the four 2D two-scale symbol relations.

**Theorem 3.1** *let* $\Phi_j, \Psi^d_{j+1}, \Psi^h_{j+1}$ *and* $\Psi^v_{j+1}$ *be defined as in equations(3.46-3.49). Then*

$$a_{mn}[\Phi_j] = 4A_{j+1,m}A_{j+1,n}a_{mn}[\Phi_{j+1}] \tag{3.56}$$

$$a_{mn}[\Psi^d_{j+1}] = 4B_{j+1,m}B_{j+1,n}a_{mn}[\Phi_{j+1}] \tag{3.57}$$

$$a_{mn}[\Psi^h_{j+1}] = 4A_{j+1,m}B_{j+1,n}a_{mn}[\Phi_{j+1}] \tag{3.58}$$

$$a_{mn}[\Psi^v_{j+1}] = 4B_{j+1,m}A_{j+1,n}a_{mn}[\Phi_{j+1}] \tag{3.59}$$

# Proof

write

$$\Phi_j = \sum_{k,\ell}^{2^{j+1}} \epsilon_{j+1,l,j+1,\ell}\Phi_j\left(cos\frac{k\pi}{2^{j+1}}\right)\sigma_{j+1,k,j+1,\ell}\Phi_{j+1} \tag{3.60}$$

and

$$a_{mn}[\Phi_j] = \sum_{k,\ell}^{2^{j+1}} \epsilon_{j+1,l,j+1,\ell}\Phi_j\left(cos\frac{k\pi}{2^{j+1}}\right)a_{mn}[\sigma_{j+1,k,j+1,\ell}\Phi_{j+1}] \tag{3.61}$$

Expanding $\epsilon_{j+1,k,\rho,\ell}$, and $\Phi_j(h_{j+1,k})$ and applying the results in lemmas 1 and 2 twice. the result in (3.56) follows. The remaining expressions are derived via identical arguments □

Observation of equations (3.56-3.59) reveals that they partitioned $V_{j+1}$ into 4 orthogonal subspaces. In the preceding sections of this chapter algorithms to decompose a DCTWM signal $f \in C(I^2)$ into each of these four components will be presented.

## 3.4 Generalized DCTWM (GDCTWM)

The DCTWM model introduced above has the advantage of simplifying implementation of algorithms and the disadvantage of allowing analysis only of DCTWM signals with equal row and column dimensions. In some application which process information blockwise, including many DCT compression and texture segmentation algorithms which analyze blocks of moderate sizes to take advantage of local correlation, it might be of practical merit to process blocks with different row and column dimensions. Chapter 5 of this thesis presents a texture segmentation algorithm based on energy measures on block of sizes $2^J + 1 \times 2^\rho + 1$, where in general $J \neq \rho$. The GDCTWM introduce below supports a MRA of signals with such dimensions.

The aim of this section is to formulate a multiresolution of $L^2_\Omega(I^2)$through generalization of DCTWM. The more generalized model is called the generalized discrete cosine wavelet model (GDCTWM) and modeled signals will be referred to as GDCTWM signals. Before proceeding, we need to properly define a few subspaces of $L^2_\Omega(I^2)$.

$$V_{J,\rho} = span\{\phi_{J,k}\phi_{\rho,\ell}\} \text{ for } k \in \{0, \cdots, 2^J\},\ \ell \in \{0, \cdots, 2^\rho\} \tag{3.62}$$

$$W^d_{j,\rho} = span\{\psi_{j+1,2r+1}\psi_{\rho+1,2\ell+1}\} \text{ for } r \in \{0,\cdots,2^j-1\},\ \ell \in \{0,\cdots,2^\rho-1\} \tag{3.63}$$

$$W^h_{j,\rho} = span\{\phi_{j,k}\psi_{\rho+1,2\ell+1}\} \text{ for } k \in \{0,\cdots,2^j\},\ \ell \in \{0,\cdots,2^\rho-1\} \tag{3.64}$$

$$W^v_{j,\rho} = span\{\psi_{j+1,2k+1}\phi_{\rho,\ell}\} \text{ for } k \in \{0,\cdots,2^j-1\},\ \ell \in \{0,\cdots,2^\rho-1\} \tag{3.65}$$

The fundamental scaling function in $\Phi_{j,\rho} \in V_{j,\rho}$ is defined as $\phi_j\phi_\rho$. The fundamental wavelets on the detailed $(W_j, \rho)$ subspaces are $\Psi^d_{j,\rho}$ which equals $\psi_{j+1}\psi_{\rho+1}$, $\Psi^h_{j,\rho}$ which equals $\phi_j\psi_{\rho+1}$ and $\Psi^v_{j,\rho}$ which equals $\psi_{j+1}\phi_\rho$. The bidimensional version of the shift operator is denoted $\sigma_{j,k,\rho,\ell}$ and the shifted bidimensional scaling function $\sigma_{j,k,\rho,\ell}\Phi_j$ is denoted by $\Phi_{j,k,\rho,\ell}$. The shifted copy of $\psi^d_{j+1,\rho+1}$ is denoted by $\Psi^d_{j+1,2k+1,\rho+1,2\ell+1}$. The same nomenclature is extended to wavelets on $W^h_{j,\rho}$ and $W^v_{j,\rho}$. Plots of a few bidimensional scaling functions and wavelets that comprised a subset of the bases functions of DCTWM are shown in figure 3.3.5.1. Basis functions present only in GDCTWM are shown in figure 3.3.5.1. We now offer without a formal proof the important result below.

$$V_{j+1,\rho+1} = V_{j,\rho} \oplus W^d_{j,\rho} \oplus W^h_{j,\rho} \oplus W^v_{j,\rho} \tag{3.66}$$

This (3.66) of course establishes the existence of MRA of $L^2_\Omega(I^2)$. The MRA of $L^2_\Omega(I^2)$is characterized by the equation below. In the next section we introduce a signal model called the GDCTWM model and present decomposition and reconstruc-

tion algorithms based on the model.

$$L^2_\Omega(I^2) = clos\{V_{0,0} \oplus \bigoplus_{j=0,\rho=0}^{\infty} W^d_{j,\rho} \oplus \bigoplus_{j=0,\rho=0}^{\infty} W^h_{j,\rho} \oplus \bigoplus_{j=0,\rho=0}^{\infty} W^v_{j,\rho}\} \tag{3.67}$$

As stated above the DCTWM deals with the special case when $j$ equals $\rho$. The GDCTWM aims to eliminate this limitation by introducing the signal model below. Let $f_{j+1,\rho+1} \in V_{j+1,\rho+1}$ be given by

$$f_{j,\rho}(x,y) = \sum_{k=0}^{2^{j+1}} \sum_{\ell=0}^{2^{j+1}} \epsilon_{j+1,k,\rho+1,\ell}\ f_{j+1,\rho+1}(k,\ell)\,[\sigma_{j+1,k,\rho+1,\ell}\,\Phi_{j+1,\rho+1}(x,y)] \tag{3.68}$$

When expressed as above we shall refer to $f_{j+1,\rho+1}$ as a GDCTWM signal. According to equation(3.66), the GDCTWM signal $f_{j+1,\rho+1}$ is decomposable into its orthogonal projections on $V_{j,\rho}$, $W^d_{j,\rho}$, $W^h_{j,\rho}$, and $W^v_{j,\rho}$. The reference [37] contains details of how this can be done. The goal of the decomposition is to obtain discrete sequences for $f_{j,\rho}(k,\ell)$, $g^d_{j,\rho}(k,\ell)$, $g^h_{j,\rho}(k,\ell)$ and $g^v_{j,\rho}(k,\ell)$. The GDCTWM theorem illustrates how the DCT transforms of these sequences are related to $F_{j+1,\rho+1}(m,n)$.

### 3.4.1 The GDCTWM Theorem

The theorem below plays a major role in DCTWM/GDCTWM signal analysis and synthesis. It is the main theorem of this thesis and is significant for several reasons. Foremost, it leads to a simple decomposition algorithm for splitting $f_{j+1,\rho+1}$

into orthogonal complements $f_{j,\rho}$, $g^d_{j,\rho}$, $g^h_{j,\rho}$ and $g^v_{j,\rho}$. The scheme depends exclusively on DCT variants for which there are an abundance of fast implementations. Furthermore, DCTs are used extensively in industry for image codecs. The advent of DCT multiscale algorithms has the potential to impact the way some existing codec standards are implemented and will certainly encourage the development of new codecs.

**Theorem 3.2** *Let* $f_{j+1,\rho} = f_{j,\rho} + g^d_{j,\rho} + g^h_{j,\rho} + g^v_{j,\rho}$ *where* $f_{j+1,\rho+1} \in V_{j,\rho}$, $f_{j,\rho} g^d_{j,\rho} \in W^d_{j,\rho}$, $g^h_{j,\rho} \in W^h_{j,\rho}$ *and* $g^v_{j,\rho} \in W^v_{j,\rho}$. *Further let*

$$f_{j,\rho} = \sum_{k,\ell=0}^{2^j} \sum_{\rho=0}^{2^\rho} \epsilon_{j,k,\rho,\ell} f_{j,\rho}(k,m)[\sigma_{j,k,\rho,\ell}\, \Phi_j] \tag{3.69}$$

$$g^d_{j,\rho} = \sum_{k=0}^{2^j-1} \sum_{\ell=0}^{2^\rho-1} g^d_{j,\rho}(k,\ell)[\sigma_{j+1,2k+1,\rho+1,2\ell+1}\, \Psi^d_{j+1}] \tag{3.70}$$

$$g^h_{j,\rho} = \sum_{k=0}^{2^j} \sum_{\ell=0}^{2^\rho-1} \epsilon_{j,k} g^h_{j,\rho}(k,\ell)[\sigma_{j,k,\rho+1,2\ell+1}\, \Psi^h_{j+1}] \tag{3.71}$$

$$g^v_{j,\rho} = \sum_{k=0}^{2^j-1} \sum_{\ell=0}^{2^\rho} \epsilon_{j,\ell} g^v_{j,\rho}(k,\ell)[\sigma_{j+1,2k+1,\rho,\ell}\, \Psi^v_{j+1}] \tag{3.72}$$

*Then,*

$$F_{j,\rho}(m,n) = \frac{F_{j+1,\rho+1}(m,n)}{4 A_{j+1,m} A_{\rho+1,n}} \quad 0 \le m \le 2^j, 0 \le n \le 2^\rho \tag{3.73}$$

$$G^d_{j,\rho}(m,n) = \frac{F_{j+1,\rho}(m,n)}{4 B_{j+1,m} B_{\rho+1,n}} \quad 2^j + 1 \le m \le 2^{j+1}, 2^\rho + 1 \le n \le 2^{\rho+1} \tag{3.74}$$

$$G^h_{j,\rho}(m,n) = \frac{F_{j+1,\rho+1}(m,n)}{4 A_{j+1,m} B_{\rho+1,n}} \quad 0 \le m \le 2^j, \quad 2^\rho + 1 \le n \le 2^{\rho+1} \tag{3.75}$$

$$G^{v}_{j,\rho}(m,n) = \frac{F_{j+1,\rho+1}(m,n)}{4\,B_{j+1,m}A_{\rho+1,n}} \quad 2^{j}+1 \le m \le 2^{j+1},\ 0 \le n \le 2^{\rho}. \tag{3.76}$$

# Proof

By the statement of the theorem $f_{j+1,\rho} = f_{j,\rho} + g^{d}_{j,\rho} + g^{h}_{j,\rho} + g^{v}_{j,\rho}$. The aim is to obtain DCTs for the discrete sequences in (3.69) to (3.72). Applying the $a_{mn}$ operator to each term in $f_{j+1,\rho+1}$ and substituting results from lemma 3.1, we arrive at the expression below.

$$\begin{aligned}
a_{mn}[f_{j+1,\rho+1}] = & \\
& \sum_{k=0}^{2^{j}}\sum_{\ell=0}^{2^{\rho}} \epsilon_{j,k,\rho,\ell} f_{j,\rho}(k,\ell)\cos(\frac{km\pi}{2^{j}})\cos(\frac{n\ell\pi}{2^{\rho}})a_{mn}[\Phi_{j,\rho}] \\
& + \sum_{k=0}^{2^{j}-1}\sum_{\ell=0}^{2^{\rho}-1} g^{d}_{j,\rho}(k,\ell)\cos(\frac{(2k+1)m\pi}{2^{j+1}})\cos(\frac{(2\ell+1)n\pi}{2^{\rho+1}})a_{mn}[\Psi^{d}_{j+1,\rho+1}] \\
& + \sum_{k=0}^{2^{j}}\sum_{\ell=0}^{2^{\rho}-1} \epsilon_{j,k}\, g^{h}_{j,\rho}(k,\ell)\cos(\frac{km\pi}{2^{j}})\cos(\frac{(2\ell+1)n\pi}{2^{\rho+1}})a_{mn}[\Psi^{h}_{j+1,\rho+1}] \\
& + \sum_{k=0}^{2^{j}-1}\sum_{\ell=0}^{2^{\rho}} \epsilon_{\rho,\ell}\, g^{v}_{j,\rho}(k,\ell)\cos(\frac{(2k+1)m\pi}{2^{j+1}})\cos(\frac{n\ell\pi}{2^{\rho}})a_{mn}[\Psi^{v}_{j+1,\rho+1}]
\end{aligned} \tag{3.77}$$

The two-scale symbols results in theorem 1 hold for DCTWM wavelets and scaling functions. Refer to remark 1 to establish corresponding GDCTWM results. Substi-

tuting the GDCTWM two-scale symbols results in (3.77) yields

$$\begin{aligned} a_{mn}[f_{j+1,\rho+1}] = & \ 4\,F_{j,\rho}(m,n)\,A_{j+1,m}A_{\rho+1,n}\,a_{mn}[\Phi_{j+1,\rho+1}] \\ & + 4\,G^{d}_{j,\rho}(m,n)B_{j+1,m}B_{\rho+1,n}\,a_{mn}[\Phi_{j+1,\rho+1}] \\ & + 4\,G^{h}_{j,\rho}(m,n)A_{j+1,m}B_{\rho+1,n}\,a_{mn}[\Phi_{j+1,\rho+1}] \\ & + 4\,G^{v}_{j,\rho}(m,n)B_{j+1,m}A_{\rho+1,n}\,a_{mn}[\Phi_{j+1,\rho+1}] \end{aligned} \tag{3.78}$$

The result in (3.76) now follows from lemma (2) □.

The above theorem points the way to GDCTWM/DCTWM decomposition and reconstruction algorithms. Pseudo codes for both are offered below.

## 3.5 Algorithms

The goal is to establish multiscale decomposition and reconstruction algorithms for analyzing 2D DCTWM and GDCTWM signals. Variants of the DCT will be required for both cases. Only GDCTWM is presented here. The DCTWM model corresponds to $j$ equals $\rho$.

### 3.5.1 GDCTWM Pseudo Algorithms

This section contains the 2-dimensional DCT transformations and the decomposition and reconstruction algorithms for GDCTWM signals. The presentation is without proof. See sections 3.3 and 3.4 for details. The constant $\Gamma_{j,\rho}$ equals $2^{\frac{2-j-\rho}{2}}$.

## The DCT Transformations

$$V_{j,\rho} \; ON \; SUBSPACE \; V_{j,\rho}$$

$$F_{j,\rho(m,n)} = \Gamma_{j,\rho} \sum_{k=0}^{2^j} \sum_{\rho=0}^{2^\rho} \epsilon_{j,k,\rho,\ell} \, f_{j,\rho(k,\ell)} \, cos\left(\frac{mk\pi}{2^j}\right) cos\left(\frac{n\ell\pi}{2^\rho}\right) \tag{3.79}$$

$$f_{j,\rho(k,\ell)} = \Gamma_{j,\rho} \sum_{m=0}^{2^j} \sum_{n=0}^{2^\rho} \epsilon_{j,m,\rho,n} \, F_{j,\rho(m,n)} \, cos\left(\frac{mk\pi}{2^j}\right) cos\left(\frac{n\ell\pi}{2^\rho}\right) \tag{3.80}$$

$$DCT - W^d_{j,\rho} \; ONSUBSPACE \; W^d_{j,\rho}$$

$$G^d_{j,\rho(m,n)} = \Gamma_{j,\rho} \sum_{k=0}^{2^j-1} \sum_{\ell=0}^{2^\rho-1} g^d_{j,\rho(k,\ell)} \, cos\left(\frac{(2k+1)m\pi}{2^{j+1}}\right) cos\left(\frac{(2\ell+1)n\pi}{2^{\rho+1}}\right) \tag{3.81}$$

$$g^d_{j,\rho(k,\ell)} = \Gamma_{j,\rho} \sum_{m=0}^{2^j-1} \sum_{n=0}^{2^\rho-1} \epsilon_{j,m,\rho,n} \, G^d_{j,\rho(m,n)} \, cos\left(\frac{(2m+1)k\pi}{2^{j+1}}\right) cos\left(\frac{(2n+1)\ell\pi}{2^{\rho+1}}\right) \tag{3.82}$$

$$DCT - W^h_{j,\rho} \text{ ON SUBSPACE } W^h_{j,\rho}$$

$$G^h_{j,\rho(m,n)} = \Gamma_{j,\rho} \sum_{k=0}^{2^j-1} \sum_{\ell=0}^{2^\rho} \epsilon_{j,k}\, g^h_{j(k,\ell)} \cos\left(\frac{(2k+1)m\pi}{2^j}\right) \cos\left(\frac{\ell n\pi}{2^\rho}\right) \tag{3.83}$$

$$g^h_{j,\rho(k,\ell)} = \Gamma_{j,\rho} \sum_{m=0}^{2^j-1} \sum_{n=0}^{2^j} \epsilon_{j,m,\rho,\ell}\, G^h_{j,\rho(m,n)} \cos\left(\frac{(2k+1)m\pi}{2^{j+1}}\right) \cos\left(\frac{n\ell\pi}{2^\rho}\right) \tag{3.84}$$

$$DCT - W^v_{j,\rho} \text{ ON SUBSPACE } W^v_{j,\rho}$$

$$G^v_{j(m,n)} = \Gamma_{j,\rho} \sum_{k=0}^{2^j} \sum_{\ell=0}^{2^\rho-1} \epsilon_{j,k}\, g^v_{j,\rho(k,\ell)} \cos\left(\frac{km\pi}{2^j}\right) \cos\left(\frac{(2\ell+1)n\pi}{2^{\rho+1}}\right) \tag{3.85}$$

$$g^v_{j,\rho(k,\ell)} = \Gamma_{j,\rho} \sum_{m=0}^{2^j} \sum_{n=0}^{2^\rho-1} \epsilon_{j,k,\rho,n}\, G^v_{j,\rho(m,n)} \cos\left(\frac{km\pi}{2^j}\right) \cos\left(\frac{(2n+1)\ell\pi}{2^{\rho+1}}\right) \tag{3.86}$$

## GDCTWM Decomposition Algorithm

*INPUT*$(j, f_{j+1,\rho+1(k,\ell)})$

*compute* $F_{j+1,\rho+1(m,n)}$ $, 0 \le m \le 2^{j+1}$ $0 \le n \le 2^{\rho+1}$

$$F_{j,\rho(m,n)} = \frac{F_{j+1,\rho+1(m,n)}}{4\, A_{j+1,m}\, A_{\rho+1,n}} \qquad 0 \le m \le 2^j,\ 0 \le n \le 2^\rho$$

$$G^{d}_{J,\rho(m,n)} = \frac{[\tau\gamma\tau\gamma F_{J+1,\rho+1}[(2^J+1:2^{J+1},2^\rho+1:2^{\rho+1})]](m,n)}{4\,B_{J+1,2^{J+1}-m}\,B_{\rho+1,2^{\rho+1}-n}} \quad 0 \le m \le 2^J-1.$$

$$0 \le n \le 2^\rho - 1$$

$$G^{h}_{J(m,n)} = -\frac{[\gamma F_{J+1}[(0:2^J,2^\rho+1:2^{\rho+1})]](m,n)}{4\,A_{J+1,m}\,B_{\rho+1,2^{\rho+1}-n}} \qquad 0 \le m \le 2^J. \quad 0 \le n \le 2^\rho - 1$$

$$G^{v}_{J(m,n)} = \frac{[\tau\gamma\tau\ F_{J+1}[(2^J+1:2^{J+1},0:2^\rho)]](m,n)}{4\,A_{\rho+1,n}\,B_{J+1,2^{J+1}-m}} \qquad 0 \le m \le 2^J-1. \quad 0 \le n \le 2^\rho$$

*compute* $f_{J,\rho(k,\ell)}$

*compute* $g^{d}_{J,\rho(k,\ell)}$

*compute* $g^{h}_{J,\rho(k,\ell)}$

*compute* $g^{v}_{J,\rho(k,\ell)}$

*OUTPUT*( $f_{J,\rho(k,\ell)}$ , $g^{d}_{J,\rho(k,\ell)}$ , $g^{h}_{J,\rho\ (k,\ell)}$ , $g^{v}_{J,\rho\ (k,\ell)}$ )

## GDCTWM Reconstruction Algorithm

*INPUT*( $J$, $f_{J,\rho\ (k,\ell)}$ , $g^{d}_{J,\rho\ (k,\ell)}$ , $g^{h}_{J,\rho\ (k,\ell)}$ , $g^{v}_{J,\rho\ (k,\ell)}$ )

*compute* $F_{J,\rho\ (k,\ell)}$

*compute* $G^{d}_{j,\rho}{}^{(k,\ell)}$

*compute* $G^{h}_{j,\rho}{}^{(k,\ell)}$

*compute* $G^{v}_{j,\rho}{}^{(k,\ell)}$

$$F_{j+1,\rho+1}(m,n) = 4\, A_{j+1,m}\, A_{\rho+1,n} F_{j,\rho}(m,n) \quad 0 \le m \le 2^j,\ 0 \le n \le 2^\rho$$

$$F_{j+1,\rho+1}(m,n) = 4\, B_{j+1,2^{j+1}-m}\, B_{j+1,2^{j+1}-n} [\gamma\tau\gamma\tau\, G^{d}_{j,\rho}](m,n)\ 0 \le m \le 2^j - 1,$$

$$0 \le n \le 2^\rho - 1$$

$$F_{j+1,\rho+1}(m,n) = -4\, A_{j+1,m}\, B_{\rho+1,2^{\rho+1}-n} [\gamma\, G^{h}_{j,\rho}](m,n) \quad 0 \le m \le 2^j,\ 0 \le n \le 2^\rho - 1$$

$$F_{j+1,\rho+1}(m,n) = -4\, B_{j+1,2^{j+1}-m}\, A_{\rho+1,n} [\tau\gamma\tau\, G^{v}_{j,\rho}](m,n) \quad 0 \le m \le 2^j - 1\ 0 \le n \le 2^\rho$$

*compute* $f_{j+1,\rho+1}{}^{(k,\ell)}$

*OUTPUT*( $f_{j+1,\rho+1}{}^{(k,\ell)}$ )

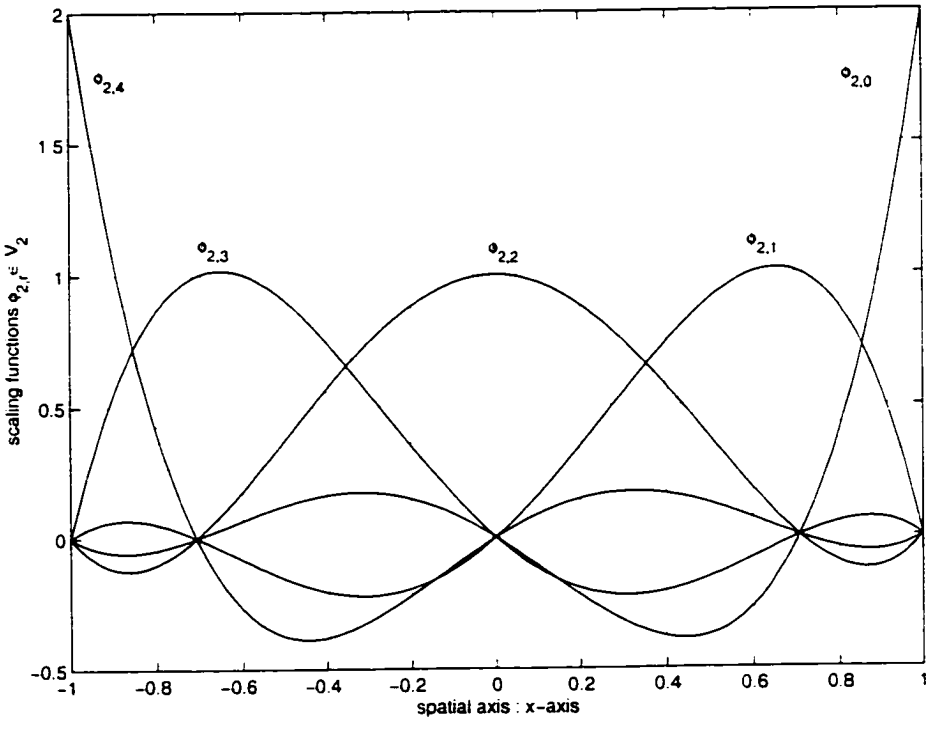


(a) scaling functions $\phi_{2,r} \in V_2$

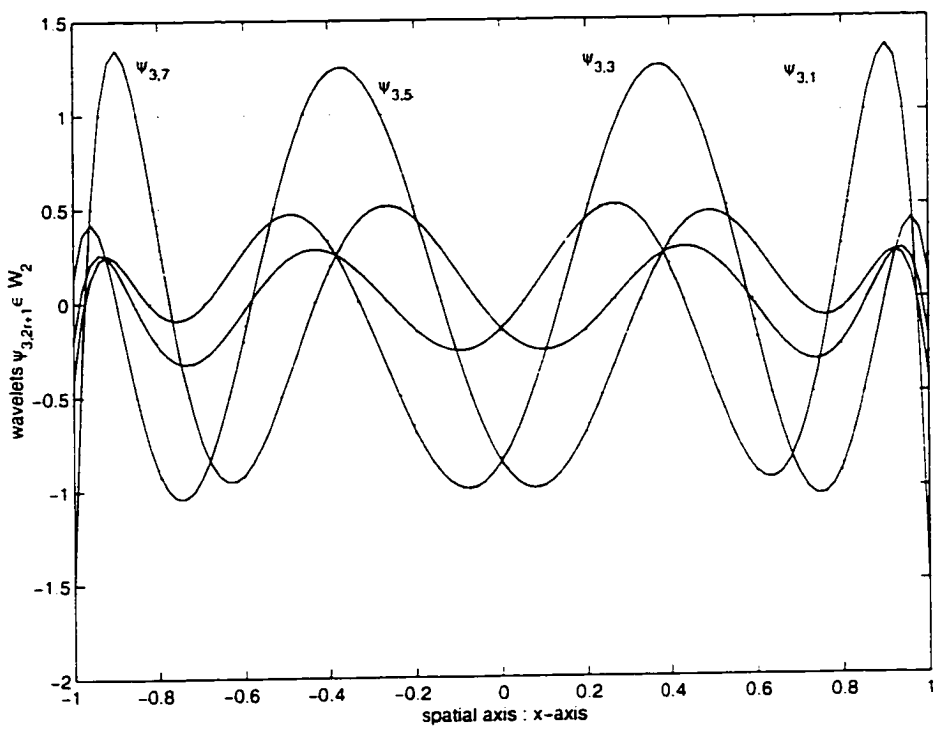


(b) wavelets $\omega_{2,r} \in W_2$

Figure 3.1: One dimensional scaling functions and wavelets spanning $V_2$ and $W_2$

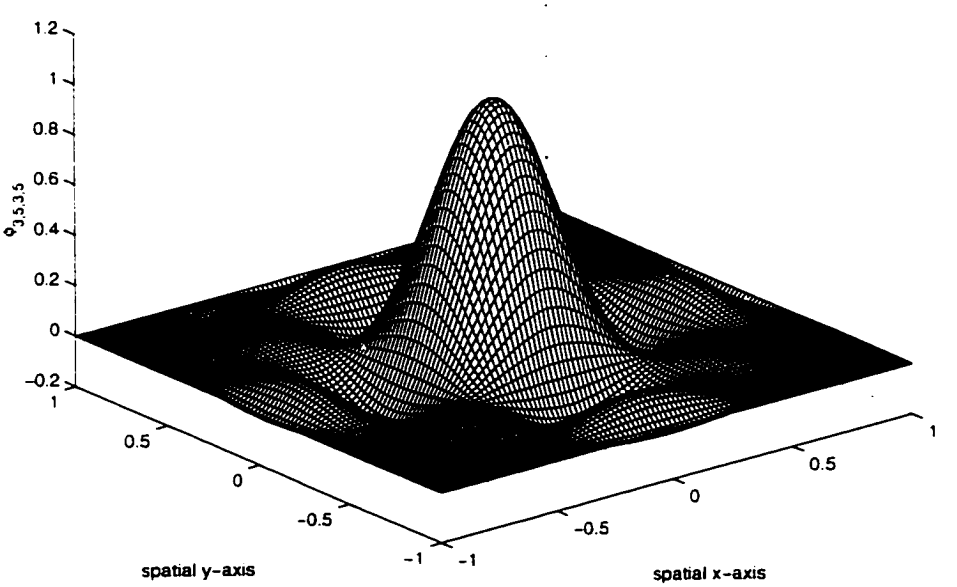


(a) scaling function $\Phi_{3,5,3,5}$

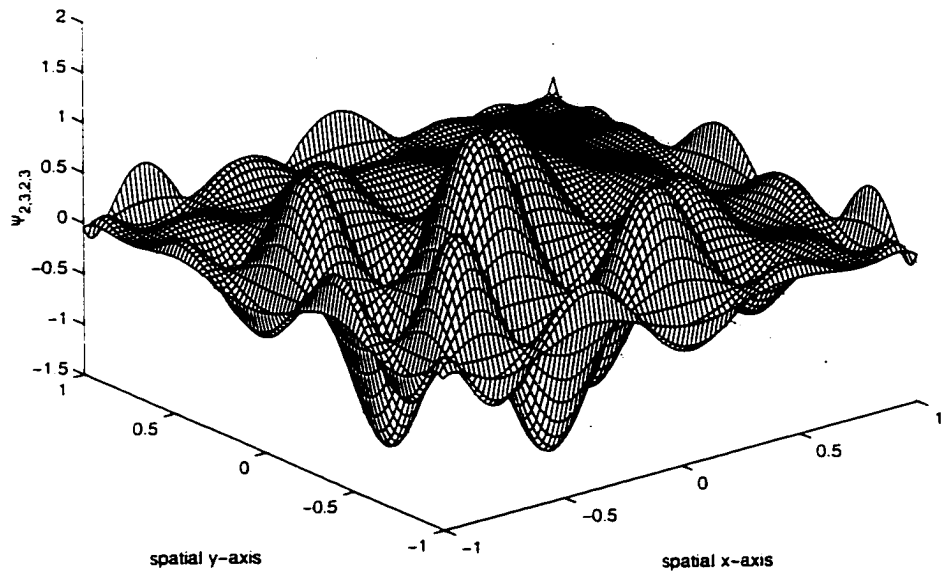


(b) wavelet $\psi_{2,3,2,3}$

Figure 3.2: Scaling functions and wavelets in $V_{3,3}$ and $W^d_{2,2}$

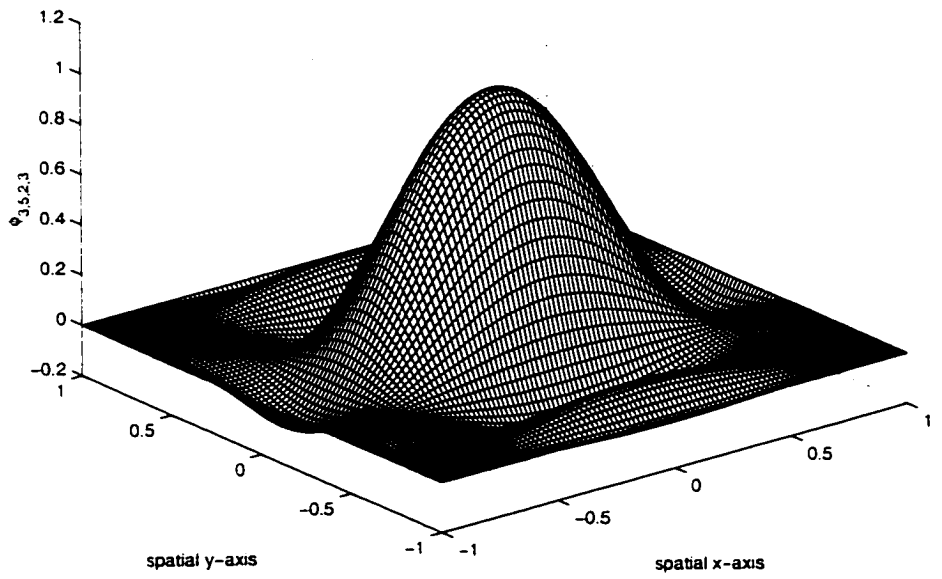


(a) scaling function $\Phi_{3,5,2,3} \in V_{3,2}$

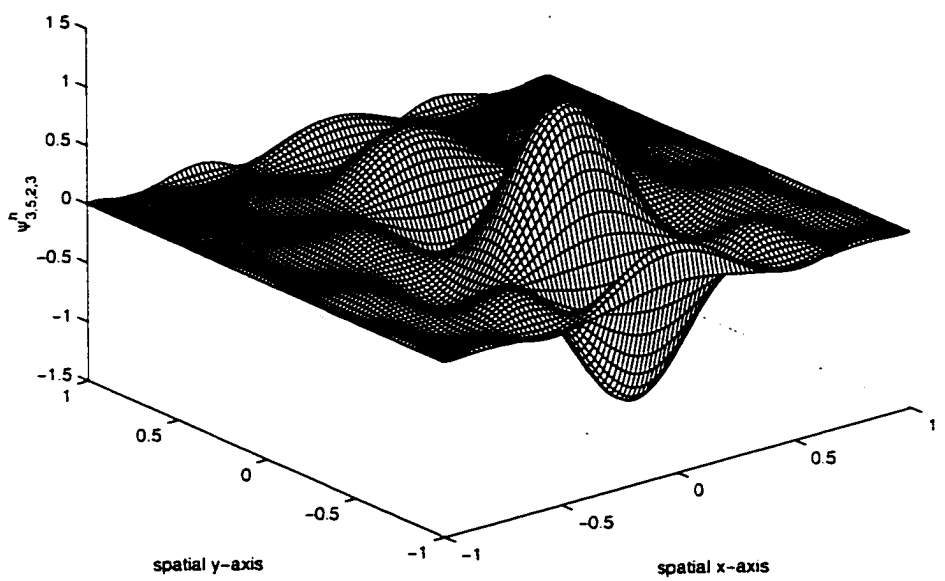


(b) wavelet $\Psi^h_{3,5,2,3} \in W^{*h}_{3,2}$

Figure 3.3: Scaling functions and Wavelets unique to GDCTWM

# Chapter 4

## Image Decomposition Applications

## 4.1 Introduction

The demand for efficient coding techniques will continue to evolve with an increasing need to transmit and store digital images. Recently, subband image coding [10]-[14] has emerged as a powerful and versatile tool in the area of data reduction. Meanwhile, coding algorithms based on transforms such as Lapped orthogonal transform [15][16] and the discrete cosine transform (DCT) [17]-[19] continue to play important roles in this field. The DCT was introduced by N. Ahmed et al.[20] as a viable alternative to the Karhunen-Leove transform [1,2] which decorrelates the input signal in the

transform domain. Today, numerous variants of the DCT are widely used in digital signal processing. Below, an orthonormal subband decomposition of $L^2(\mathbb{R}^2)$ using a filter bank is reviewed and an image decomposition application using DCTWM for signals $S \in L^2_\Omega(I^2)$ is presented. The DCT-based decomposition of $L^2_\Omega(I^2)$ and the orthonormal decomposition of $L^2(\mathbb{R}^2)$ are compared for their energy packing efficiency. Finally, some consideration is given to the computational complexities of both methods.

## 4.2 Decomposition Methods

Two methods of signal decomposition will be examined below, filter banks related decomposition and GDCTWM based decomposition. First, subband decomposition has become an integral tool in signal processing applications such as frequency domain speech scrambling, image compression[48] [49][50][51] and signal enhancement[52][53]. The ultimate objective in subband decomposition is to split the input signal into subbands. This is usually followed by decimation to remove redundancies present in the subbands. Specifically, when a M-channel filter bank is employed decimation by a factor of M is performed. This means that one of every M samples of a filtered output of the analysis subsystem is retained. The decimated outputs are interpolated

or up-sampled and sent to the synthesis subsystem for reconstruction. The synthesis filters are chosen so that $\hat{x}(n) = x(n-m), m \in \mathbb{Z}$. To date a number of solutions for the analysis and synthesis filters have been proposed([54] -[60]). The orthonormality constraint for perfect reconstruction(PR) filter banks imposes the following modulation domain relations on the analysis and synthesis filters[31-32].

$$H_0(z)H_0(z^{-1}) + H_0(-z)H_0(-z^{-1}) = 2 \tag{4.1}$$

$$H_1(z) = -z^{1-2k}H_0(-z^{-1}), \quad k \in \mathbb{Z} \tag{4.2}$$

$$G_i(z) = H_i(-z^{-1}), \quad i = 0, 1 \tag{4.3}$$

The connection between the continuous wavelet transform and filter bank is well documented([61] -[40]). In this work interest is given only to filter banks giving rise to an orthonormal multiresolution of $L^2(\mathbb{R})$. In those cases the scaling functions and wavelets are related to $h_0(n)$ and $g_0(n)$ by

$$\phi(x) = \sqrt{2}\sum_{n\in\mathbb{Z}} h_0(n)\phi(2x-n) \tag{4.4}$$

$$\psi(x) = \sqrt{2}\sum_{n\in\mathbb{Z}} g_0(n)\phi(2x-n) \tag{4.5}$$

The regularity of $\phi$, and hence that of $\psi$, is regulated by the number of zeros of $H_0(z)$ at z= -1. The greater the number of zeros, the greater is the regularity. Regularity is a measure of smoothness. The regularity of $\phi$ equals $m + \alpha$ if $\phi$ is m times differentiable and $\phi^m$ is Hölder continuous of order $\alpha$. Closely related to

regularity, the number of vanishing moments of $w$ equals N, where N is the number of zeros of $H_0(z)$ at z = -1. This means that

$$\int_{\mathbf{R}} x^n \psi(x)\, dx = 0, \quad n = 0, 1, \cdots, N-1. \tag{4.6}$$

It has been reported that compression of N times differentiable functions can be done most efficiently using wavelets with N vanishing moments. For the purpose of compression, the basic filter bank structure of figure 2.1 is iteratively applied to further split the subband signals. It is not uncommon to have as many as six to eight levels in typical applications. The subband signals are then separately encoded. An equivalent analysis can be extended to $L^2(\mathbb{R}^n)$ via the tensor product. The filter bank used, first proposed in [6], is shown in figure 4.5.2. Assuming the orthonormal case, a theoretical feature of the analysis is that the energy in the input signal is precisely preserved in the subband signals. That is

$$\mathbb{E}(S_j) = \mathbb{E}(S_{j-1}) + \mathbb{E}(S^h_{j-1}) + \mathbb{E}(S^d_{j-1}) + \mathbb{E}(S^v_{j-1}), \tag{4.7}$$

where $\mathbb{E}$ is the energy operator. Practically (4.7) is not generally realized since decimation in the analysis subsystem inevitably introduce edge effects. Edge effects refer to the distortion which occurs on the boundary of the reconstructed image $\hat{S}_j$. The problem is typically handled by periodically extending the input signal. Although this solution may eliminate the boundary distortion, it also complicates

| Properties | GDCTWM | 2-Channel Filter Bank |
|---|---|---|
| Available fast implementation | yes | yes |
| Recursive | yes | yes |
| Induces edge distortion | no | yes |
| Multiwavelets | yes | no |
| Subband-splitting | no | yes |
| Energy preserving | yes | yes |

Table 4.1: Comparison of GDCTWM and 2-Channel subband decompositions

the compression of high frequency bands of some images[63]. In the above analysis it is assumed that the reference image $S \in L^2(\mathbb{R}^2)$.

GDCTWM decomposition is based on results from interpolating wavelets theory. The main results were presented in chapter 3. For a signal $S \in L^2_\Omega(I^2)$, a multiresolution decomposition of S is implemented using DCT variants as discussed in chapter 3. This method has several advantages as compared with the filter band subband scheme. Table 4.1 compares both methods. Note that in practice only GDCTWM preserves 100 percent of the input energy. For all the images decomposed using both schemes the output images visual quality, apart from edge distortion, looks the same to the naked eye.

## 4.3 Proposed Image Model

The multiresolution of $L^2_\Omega(I^2)$ has already been characterized in chapter 3. Let $S \in L^2_\Omega(I^2)$ be an image targeted for analysis. Further suppose that S is represented as a GDCTWM signal. It is shown that the GDCTWM representation is a useful alternative to the $L^2(\mathbb{R}^2)$ representation which assumes that S can be written as the summation of scaled-shifted scaling functions as in

$$S_j = \sum_{j \in Z} a_{j,n} \varphi_( 2^j x - n). \tag{4.8}$$

As in chapter 3 . the GDCTWM representation is defined by

$$S_{j+1} = \sum_{k,\ell=0}^{2^{j+1}} \epsilon_{j+1,k,j+1,\ell}\, s_{j+1}(k,\ell)[\sigma_{j+1,k,j+1,\ell} \Phi_{j+1}], \tag{4.9}$$

where the coefficients $s_{j+1}(k,\ell)$ are the samples of $S_{j+1}$ given by $S(h_{j+1,k}, h_{j+1,\ell})$. The signal $S_{j+1}$ can be written in terms of its projection on orthonormal subspaces $V_j, W_j^d, W_j^h$ and $W_j^v$. The aim is to decompose S into orthonormal components as in $S_{j+1} = S_j + S_j^d + S_j^h + S_j^v$. Analysis and synthesis are realized via the decomposition and reconstruction algorithms of chapter 3. Block diagram structures for both algorithms are portrayed in figure 4.3. Unlike the filter bank case, the signals $S_j$, $S_j^d$, $S_j^h$, and $S_j^v$ are not theoretically confined to separate frequency subbands. However, like the

filter bank case.

$$\mathbb{E}(S_{J+1}) = \mathbb{E}(S_J) + \mathbb{E}(S_J^d) + \mathbb{E}(S_J^h) + \mathbb{E}(S_J^v), \tag{4.10}$$

a consequence to the orthonormality of the transformation.

In actual implementation, the available samples $s_{J+1}(k, \ell)$ are interpreted as the projection coefficients of some $S \in L^2_\Omega(I^2)$ on $V_j$. This practice has already become standard in most application of the discrete wavelet transform when only samples of the signal are available. Repetition of the scheme in figure 2.1 generates the MRA pyramid of lower resolution images $S_{J-j}$, $j = 0, 1, \cdots, L-1$, where L is the number of levels in the MRA pyramid. The images $S^d_{J-j}$, $S^h_{J-j}$, and $S^v_{J-j}$ are the detailed components which can be used to reconstruction $S_{J-j+1}$ given $S_{J-j}$. GDCTWM decomposition differs from subband decomposition in two important respects. First, the signals on a given level in the pyramid are not constrained to reside in separate frequency subbands. Secondly, the bases functions for the transformation is fixed for a given image size. This makes the filter bank paradigm more versatile, as the filters in the bank dictate the outcome. However, this is not a serious drawback of GDCTWM representation as one the main goals of any transformation is data reduction and the DCT-based scheme will perform at least as satisfactorily as a filter bank model for compressing a large class of signals. Moreover, the GDCTWM

scheme is amendable to VLSI implementation and there are many fast computational algorithms to chose from, depending on application([64] -[69]). The next section examines the energy compaction property of the GDCTWM and filter bank models.

## 4.4 GDCTWM and Energy Compaction

The Karhunen-Leove transform(KLT) has been shown to be statistically optimal with respect to minimizing the mean square error(MSE) for the class of Markov-1 signals [66][70][71] . When S is such a signal its auto-covariance matrix $\Phi$ is of the form

$$\Phi_s = E[S\,S^T](j,k) = \rho^{|j-k|}, \tag{4.11}$$

where E is the expectation operator and $\rho$ is the correlation coefficient between adjacent entries in the vector S. The KLT diagonalizes $\Phi$ and the truncated MSE is given by

$$\epsilon = \sum_{j=N+1} u_j, \tag{4.12}$$

where $u_j$ is the $j^{th}$ eigen-value of $\Phi_s$. Clearly then, $\epsilon$ (4.12) can be minimized by rearranging the eigen-values in descending order as in $u_0 > u_1 > \ldots > u_N > u_{N+1} > \ldots$ , and truncating the sum after, say, N terms. One interpretation of the above

result is that KLT packs the most energy in the fewest transformed coefficients and thus the KLT is optimal for data compression. However, KLT is signal dependent and hence ideal but not practical. This fact has been the impetus behind the search for other unitary transforms[3-6] which are asymptotically equivalent to KLT. As it turns out the DCT-II and the DCT-I are asymptotically equivalent to KLT, the former in the sense as $\rho \rightarrow 1$ and the latter in the sense as the parameter(image size ) $J \rightarrow \infty$[70][71]. In fact, in terms of energy packing efficiency the DCTs are second only to KLT for a large class of signals[72]. This explains the popularity of DCTs in practical applications.

Based on the above argument, the proposed DCT-based multiresolution decomposition scheme ought to perform at least as well as the orthonormal filter bank subband decomposition if the goal is data reduction. To indirectly support this conjecture, both schemes are compared for their modified energy packing efficiency(MEPE) defined as

$$MEPE(S_{J-j}) = \frac{\mathbb{E}(S_{J-j})}{\mathbb{E}(S_J)}, \tag{4.13}$$

where $\mathbb{E}$ is the energy operator, $S_J$ the original reference image, and $S_{J-j}$ is the reference image on level $j$ in the MRA pyramid. The MEPE is unity for $j = 0$ and strictly less than unity otherwise. The motivation for using (4.13) as a performance

measure hinges on the fact that if $MEPE \rightarrow 1$, then the energy in each of the three detail images $S^0_{J-J}$, $S^1_{J-J}$, and $S^2_{J-J}$ must be small and thus these images could be coded using few bits. This observation is in accordance with (4.10) which leads to the relation.

$$MEPE(S_{J-J}) + MEPE(S^0_{J-J}) + MEPE(S^1_{J-J}) + MEPE(S^2_{J-J}) = 1. \quad (4.14)$$

Also, a large MEPE suggests that $S_{J-J}$ retains the dominant structural features from $S_J$. Other more elaborate performance measures have been suggested and thoroughly investigated. These include the *energy packing efficiency*[72], *fractional correlation* [66] which measures the post transform residual correlation, and *rate distortion*[73] which measures the number of bits per transformed coefficient required for coding subject to a specified allowable average distortion. The objective here, however, is limited and as no actual coding is done, the MEPE will suffice.

Empirical data is obtained as follows. Each image in figure 4.1 is decomposed using both the proposed algorithm and filter banks based on $Daub_6$ and $Daub_{10}$ filters. The filters are chosen for their orthonormal property and the number of vanishing moments. The coefficients for the filters are given in table 4.5.2. The images are chosen for the difference in their statistical properties. In each case decomposition was performed up to 6 levels. The reference images are shown in figure4.5.2. The

MEPEs are computed and plotted in figure 4.5.2. It is clear that the lower resolution GDCTWM signal retains a greater fraction of the original signal than the corresponding filter bank outputs using $Dau_4$ or $Dau_{10}$.

## 4.5 GDCTWM Implementation Considerations

Four variants of the DCT are involved in the GDCTWM decomposition and reconstruction algorithms in chapter 3: classical DCT-I and DCT-II, and two variants consist of a composition of both. Because DCTs are computationally expensive, much research have been conducted into fast DCT implementations. The algorithms which emerged can be categorized into two groups. Algorithms in the first group are based on decimation in time where as algorithms in the other are based on decimation in frequency. Algorithms can further be categorized as recursive or non-recursive. Much of the research done to date paid attention to recursive algorithms which attempt to reduce a $N \times N$ DCT to a $\frac{N}{2} \times \frac{N}{2}$ DCT computation.

The DCT-II is the most researched of the two classical variants and many fast DCT-II algorithms are available. Fast DCT-1 algorithms are not as common. Since the main variant involved in the GDCTWM algorithms is the DCT-1, this section briefly

focuses on two efficient DCT-1 implementations. The presentation is for the one-dimensional case but the results can readily be extended to two dimension.

### 4.5.1 A decimation in time DCT-I

The classical one dimensional DCT-1 coefficients of the discrete sequence $s_{J+1}$ are defined by

$$(C^I S_J)(m) = \sum_{k=0}^{2^{J+1}} \epsilon_{J+1,k}\, s_{J+1}(k) cos(\frac{mk\pi}{2^{J+1}}) \quad 0 \leq m \leq 2^{J+1}. \tag{4.15}$$

where the normalization factor is dropped for simplicity. A direct realization of 4.15 requires $2^{J+2}$ addition and an equal number of multiplication. When $J$ is large this cost is prohibitive for practical applications. A decimation in time algorithm to compute (4.15) is presented below. The computational cost is shown in table 4.5.2.

$$(C^I s_{J+1})(m) = (C^I_J s^r_J)(m) + (C^{II} s^d_J)(m) \tag{4.16}$$

$$(C^I s_{J+1})(2^{J+1} - m) = (C^I s^r_J)(m) - (C^{II} s^d_J)(m) \tag{4.17}$$

$$(C^I s_{J+1})(2^J) = (C^I s^r_J)(2^J) \tag{4.18}$$

where

$$s^r_J(m) = s_{J+1}(2m) \tag{4.19}$$

$$s_j^d(m) = s_{j+1}(2m+1) \quad 0 \le m \le 2^j \tag{4.20}$$

### 4.5.2 A decimation in frequency DCT-I

The next DCT-I algorithm, which is based on decimation in frequency, is slightly less efficient that the decimation in time algorithm above. The improvement over a direct implementation is, however, significant.

$$(C^I s_{j+1})(2m) = (C^I s_j^+)(m) \tag{4.21}$$

$$(C^I s_{j+1})(2m+1) = (C^{III} s_j^-)(m) \tag{4.22}$$

where

$$s_j^+(k) = s_{j+1}(k) + s_{j+1}(2^{j+1} - m) \quad 0 \le m \le 2^j \tag{4.23}$$

$$s_j^-(k) = s_{j+1}(k) - s_{j+1}(2^{j+1} - m) \quad 0 \le m \le 2^j - 1 \tag{4.24}$$

See table 4.5.2 for cost comparison to the decimation in time algorithm.

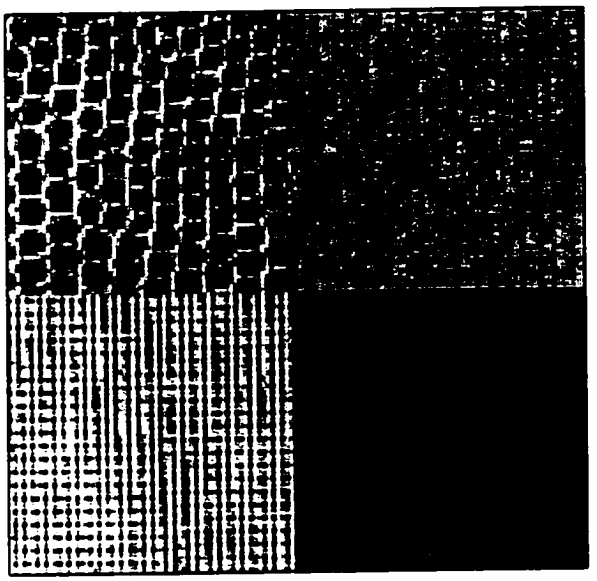

(a)

(b)

Figure 4.1: Original images (a) 129x129 texture image (b) 513x513 Mandrill image

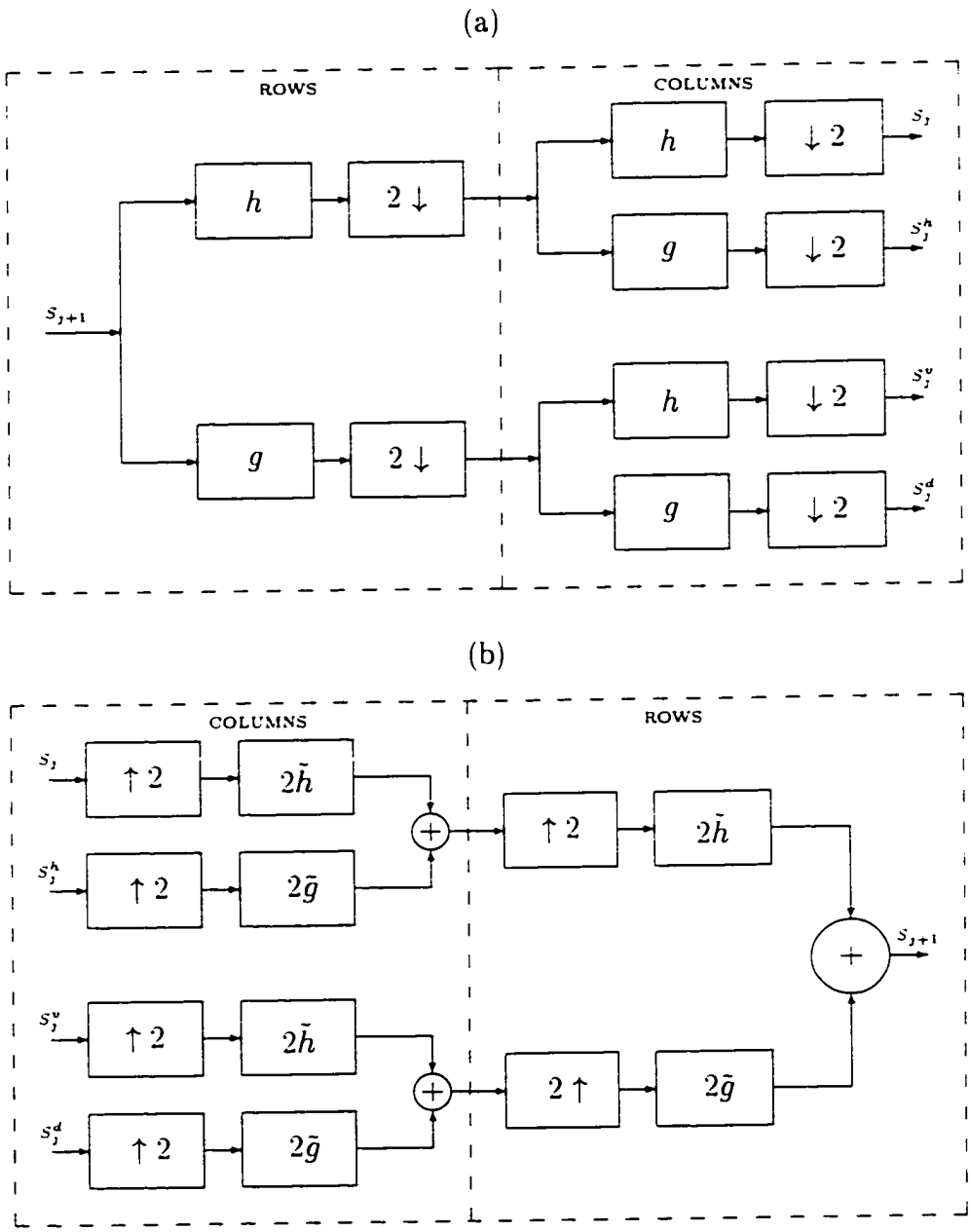


Figure 4.2: MRA of $S_{j+1}$ via filter bank. (a) Decomposition (b) Synthesis

| Algorithms | Addition | Multiplication |
|---|---|---|
| Decimation in time algorithm | $(\frac{3N}{2}+1)\,log_2(N)-2N+4$ | $(\frac{N}{2})\,log_2(N)-N+1$ |
| Decimation in frequency algorithm | $(\frac{3N}{2}+2)\,log_2(N)-2N+4$ | $(\frac{N}{2})\,log_2(N)-N+1$ |

Table 4.2: Computational cost comparisons for $N = 2^J$.

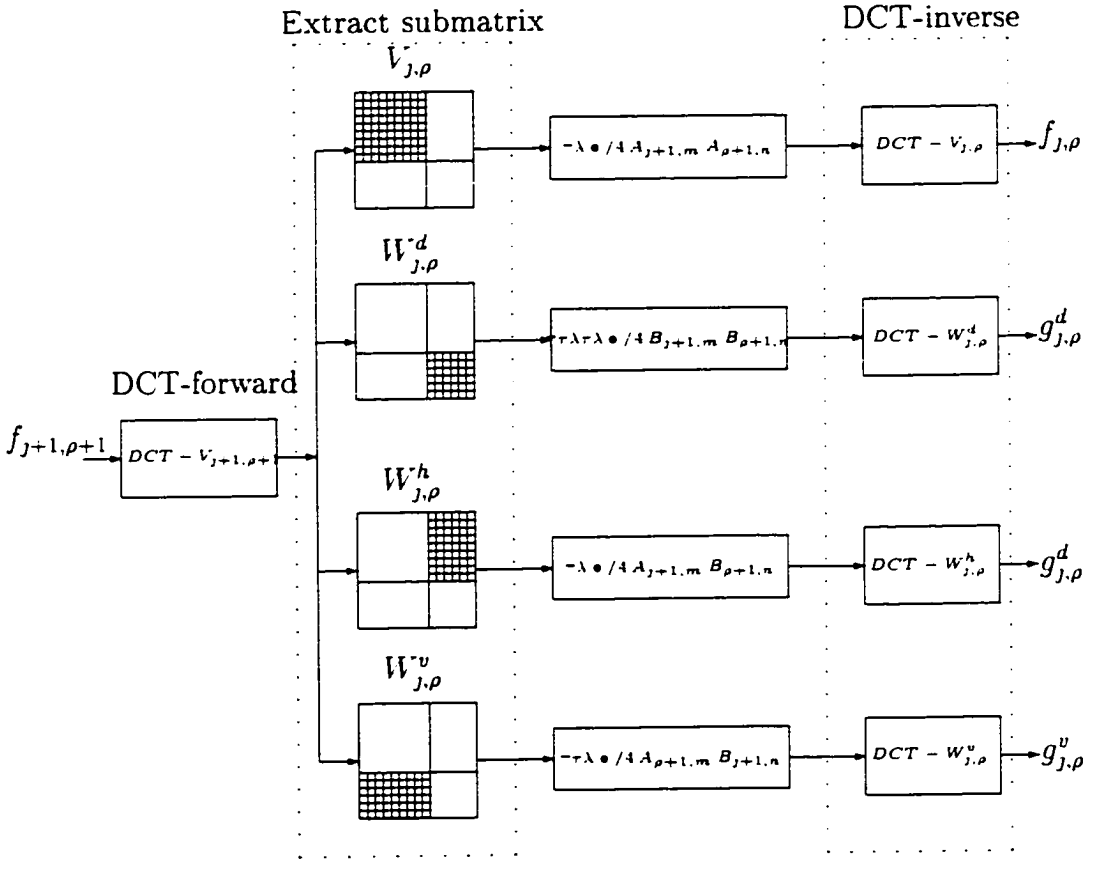


(a) GDCTWM DECOMPOSITION

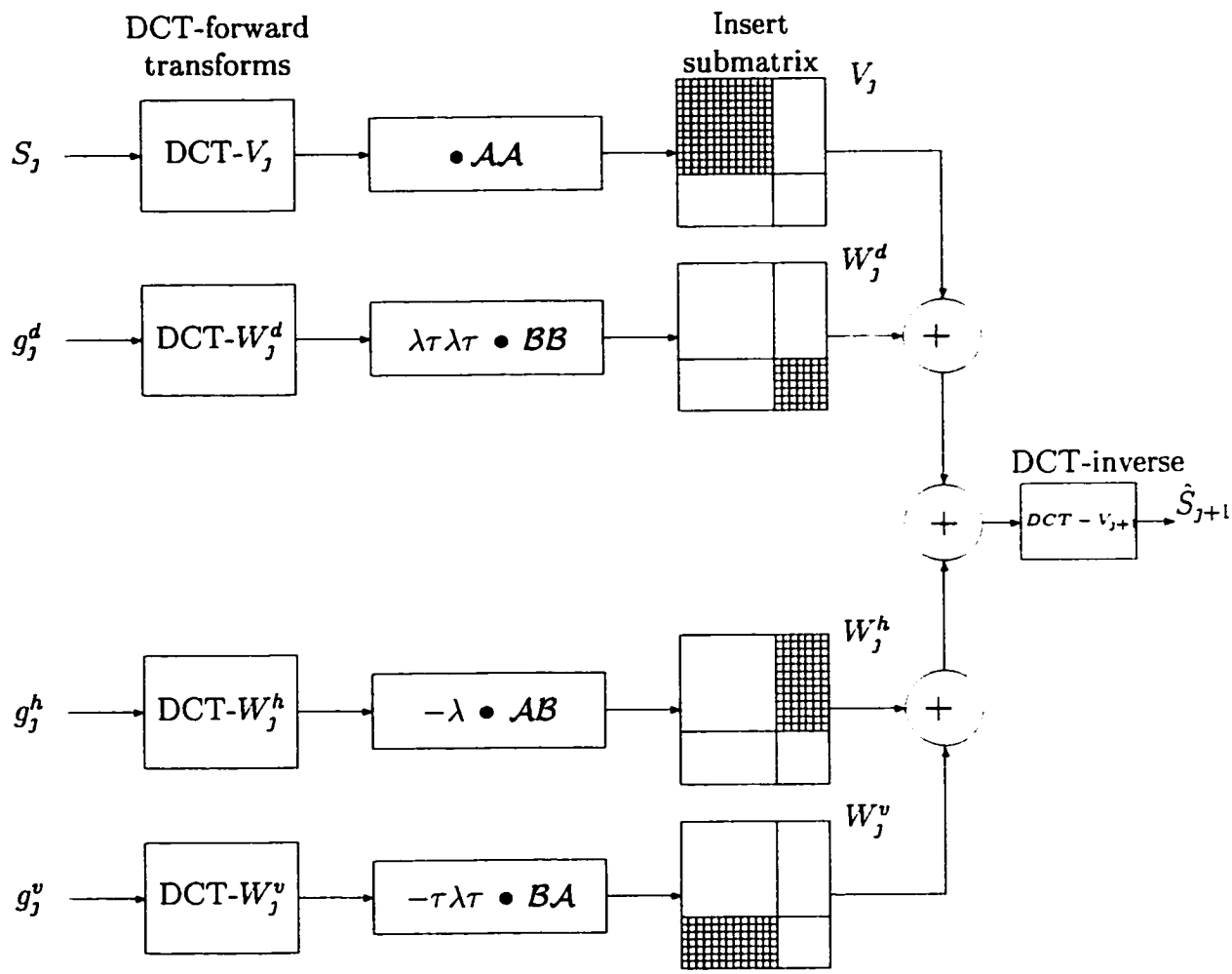


(b) GDCTWM SYNTHESIS

Figure 4.3: GDCTWM Analysis. (a) Decomposition (b) Synthesis

| n | $Daub_4$ coefficients | $Daub_{10}$ coefficients |
|---|---|---|
| 0 | 0.230377813309 | 0.026670057901 |
| 1 | 0.714846570552 | 0.188176800078 |
| 2 | 0.630880767930 | 0.527201188931 |
| 3 | -0.027983769417 | 0.688459039454 |
| 4 | -0.187034811719 | 0.281172343662 |
| 5 | 0.030841381836 | -0.249846424325 |
| 6 | 0.032883011667 | -0.195946274375 |
| 7 | -0.010597401785 | 0.127369340337 |
| 8 | | 0.093057364604 |
| 9 | | -0.071394147166 |
| 10 | | -0.029457536821 |
| 11 | | 0.033212674059 |

| n | $Daub_4$ coefficients | $Daub_{10}$ coefficients |
|---|---|---|
| 12 | | 0.003606553566 |
| 13 | | -0.010733175483 |
| 14 | | 0.001395351747 |
| 15 | | 0.001992405295 |
| 16 | | -0.000685856694 |
| 17 | | -0.000116466855 |
| 18 | | 0.000093588670 |
| 19 | | -0.000013264203 |

Table 4.3: Coefficients of Daubechies' filters used in simulation

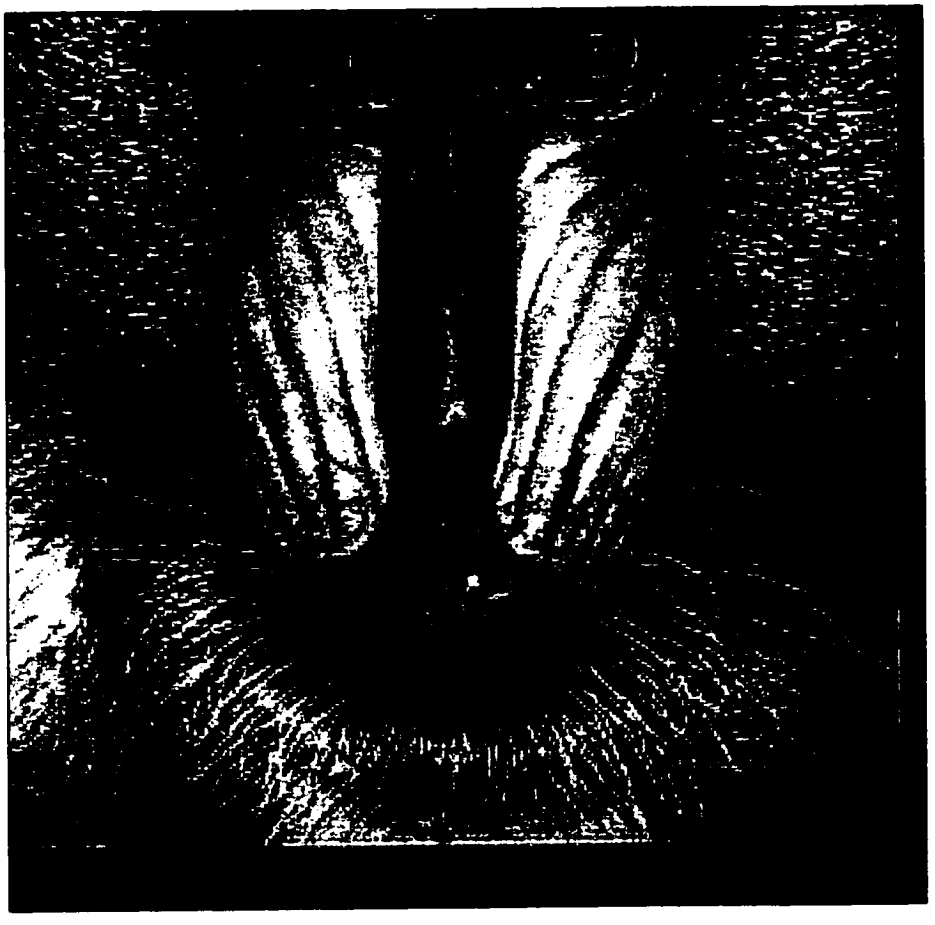

(a) GDCTWM: 1

(b) Filter Bank: 1

Figure 4.4: Decomposition results using the GDCTWM model and filter bank model.

(a) Level 1 mandrill image(GDCTWM) (b) Level 1 mandrill image (Filter Bank)

(a) GDCTWM: 2

(b) Filter Bank: 2

Figure 4.5: Decomposition results using the GDCTWM model and filter bank model.

(a) Level 2 mandrill image(GDCTWM) (b) Level 2 mandrill image (Filter Bank)

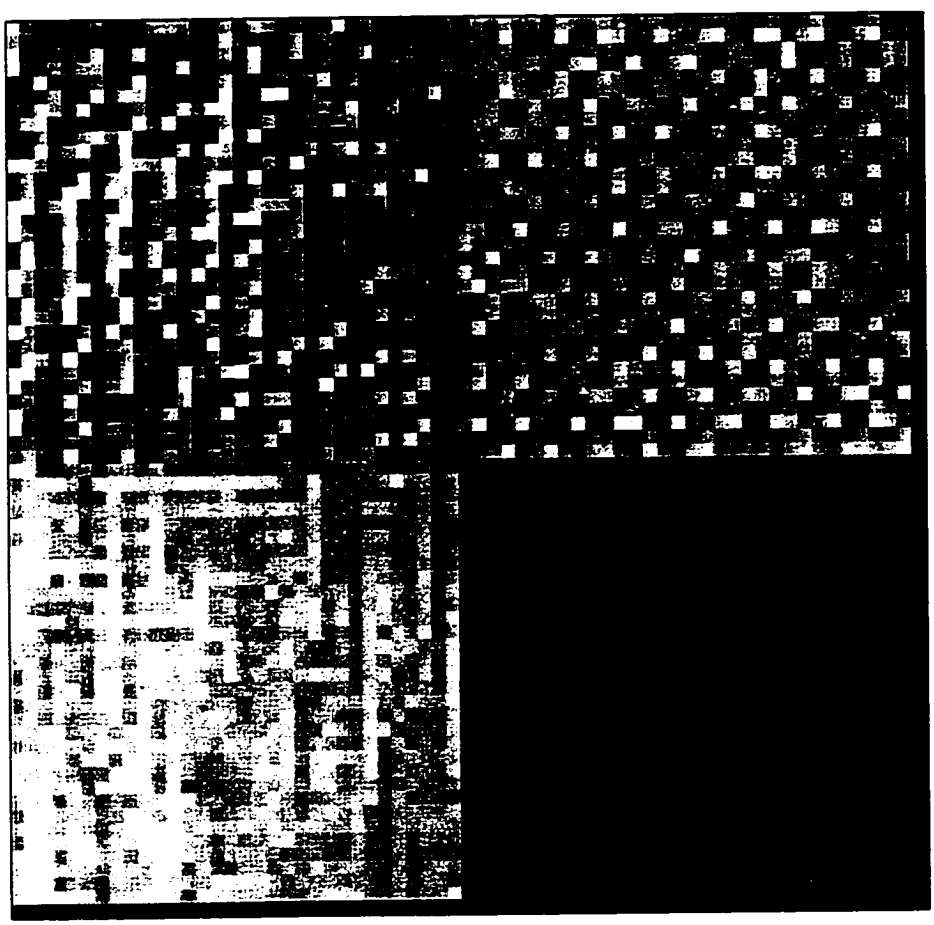

(a) GDCTWM: 1

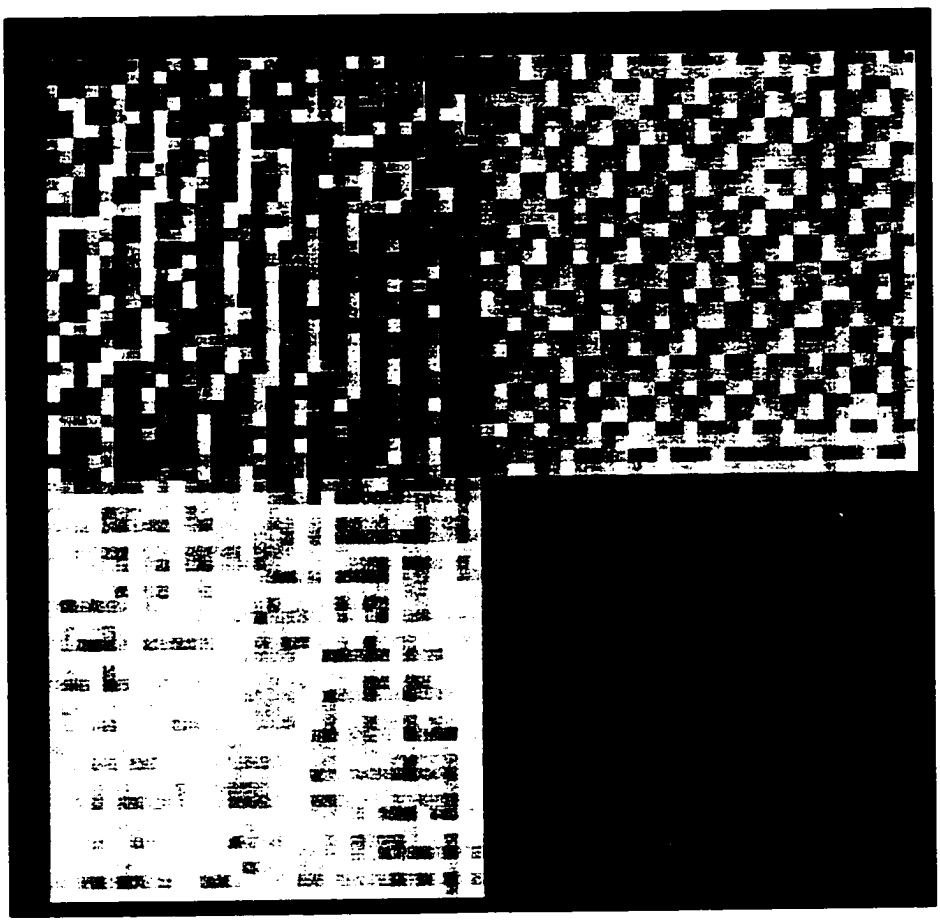

(b) Filter Bank: 1

Figure 4.6: Decomposition results using the GDCTWM model and filter bank model.

(a) Level 1 texture image(GDCTWM) (b) Level 1 texture image (Filter Bank)

(a)

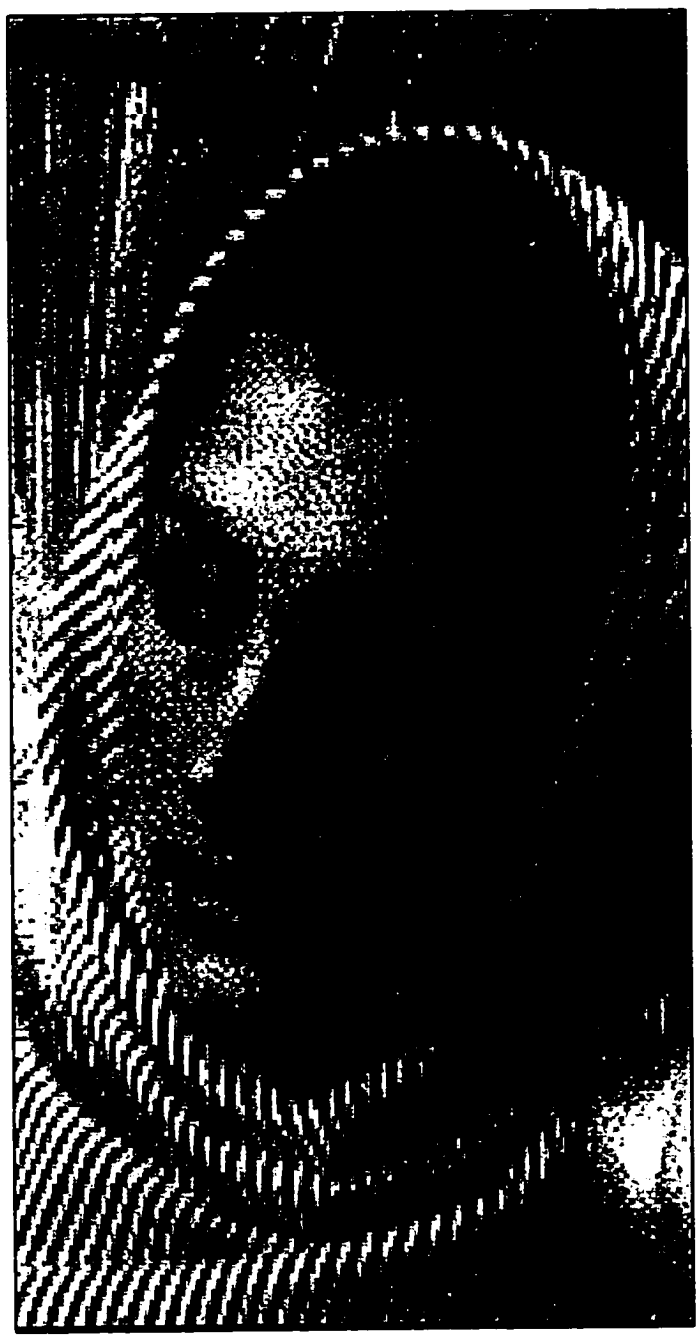

(b)

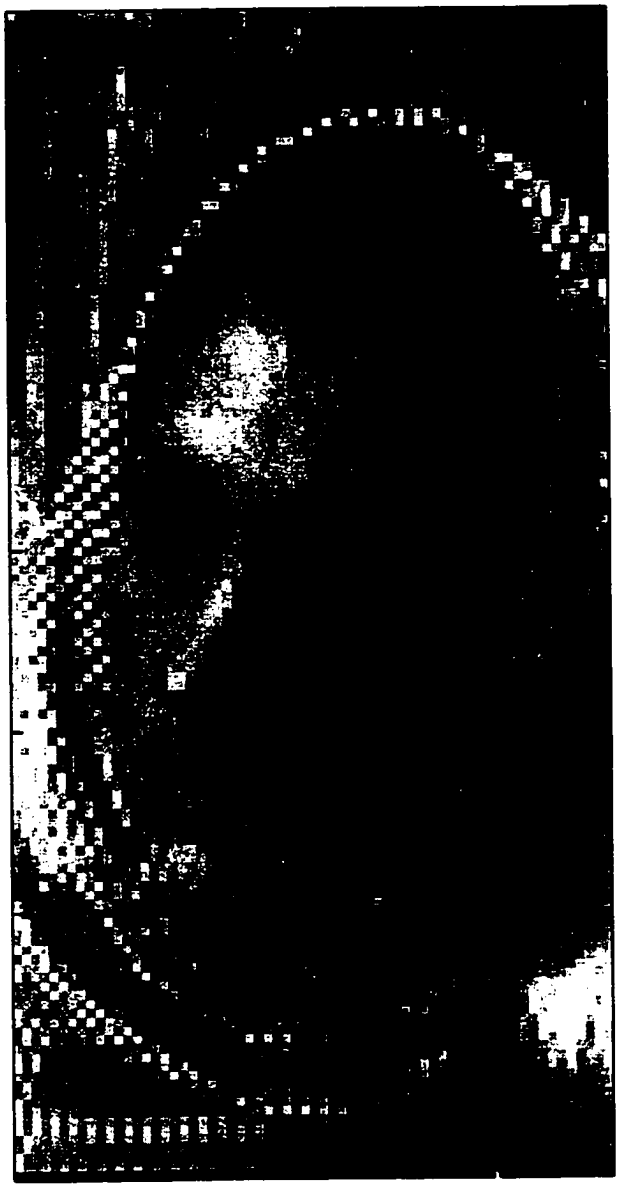

(c)

Figure 4.7: MRA of Block segment (a) Original image $f_{8,8}$. (b) block segment $f_{8,7}$. (c) derived lower resolution GDCTWM signal $f_{7,6}$.

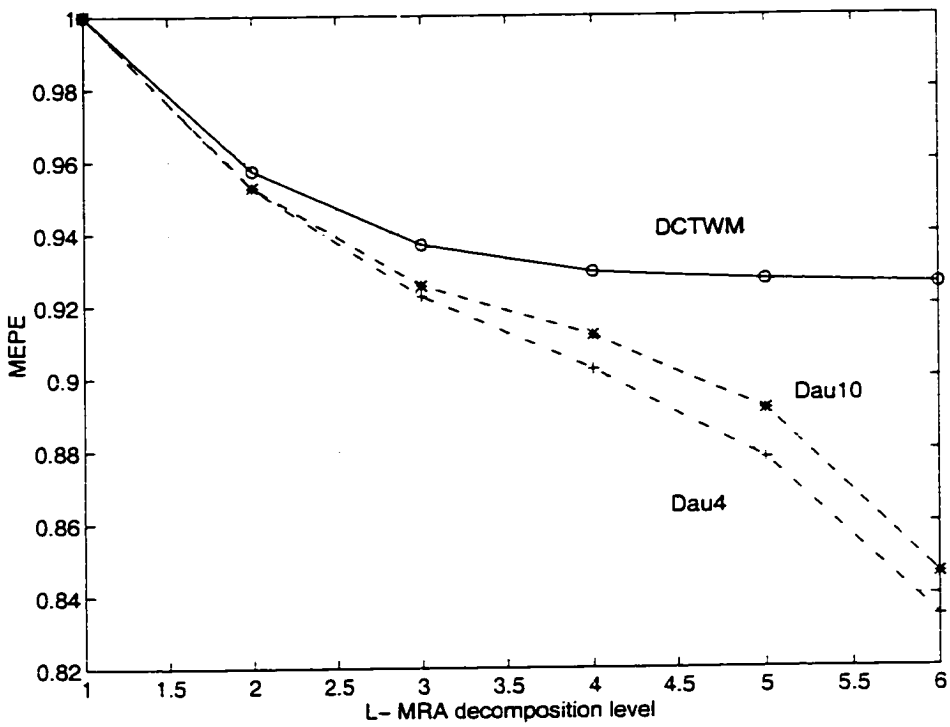


(a)

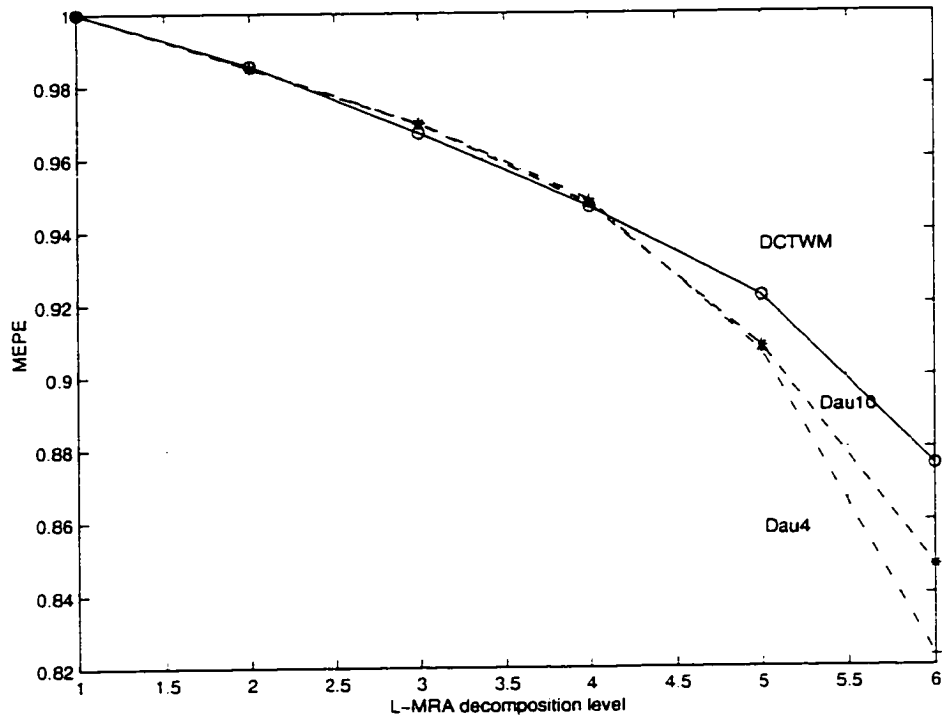


(b)

Figure 4.8: Comparison of MEPE for wavelets:(1) $+\ dau_4$ (2) $*\ dau_{10}$ (3) $o\ DCTWM$. (a) Results for texture image in figure 4.1 (b) Results for Mandrill image in figure 4.2

# Chapter 5

## Texture Segmentation

## 5.1 Introduction

Texture segmentation is an essential step in many image processing applications, including object recognition, data classification and compression, image restoration and artificial intelligence. Segmentation involves partitioning an image into regions, each region having distinct features allowing it to be discriminated from every other region. It is the goal of any segmentation algorithm to identify features in an image which can be utilized by a data clustering algorithm for regional identification and segmentation. Traditionally, there are two main approaches of modeling an image in

order to extract discriminatory features. The structural model assumes that a texture is composed of texels, patches of well-defined shape and luminance characteristics arranged periodically in perhaps one or more orientations. It is essential to note that at this time that not all textures can be modeled as described above. Some texture are void of clearly recognizable texels and may n fact lack features oriented in any particular direction. However, different textures possess inherent distinctive features irrespective of the occurrence of texels. For cases where the structural model is inadequate, a statistical model is most often used. In statistical image segmentation a texture is usually modeled as a random field, a common choice being a Markov random field, with parameterized distributions. The segmentation problem is then transformed into the estimation of distributions parameters.

The fact that optimal estimation algorithm often requires large data sets for reliable parameter estimation has often been sited as a drawback of the statistical approach. Nonetheless, a number of successful random field models have been proposed[22] [74][75]. Recently, Speis and Healey proposed a random model whose spatial interaction is a random field[76]. There it is reported that the size of the sample required for satisfactory parameter estimation to be as small as a 16x16 image segment. The proposed model is able to make use of any local spatial information and initial results indicates that performance is comparable to other well known models, such as

Guassian random field and Markov random field(MRF).

## 5.2 Feature Extraction Methods

The two main approaches to texture modeling gives rise to two methods of feature extraction. As stated earlier statistical models generally utilize random fields which are not discuss here. Typically, for structural models, features are often extracted by convolving an image I with filters $g_i$ tailored to be maximally correlated with texels elements in the image. That is, take

$$f_j(t) = \| \int_{\mathbb{R}^2} I(\tau)\, g_j(\tau - t)\, dt \| \tag{5.1}$$

where $f_j(t)$ is interpreted as a feature in I at location $t \in \mathbb{R}^2$. When the $g_j s$ are Gabor elementary functions(GEF), it is not uncommon to tune the filters $g_j$ to frequencies $(U_i, V_i)$ and orientations $\theta_i$, $i = 1, 2, \cdots, N$. The number of filters N corresponds to the number of features per location. However, one may choose a set of elementary functions satisfying

$$\sum_{i=1}^{N} G_j(\omega) = 1, \tag{5.2}$$

where $G_j(\omega)$ is the Fourier transform of $g_j$. The filters described in section IV satisfy 5.2 as do filters in a classical orthogonal filter bank. Typically, a N-dimensional

feature vector

$$f(t) = [f_1(t), f_2(t), \ldots . f_N(t)] \tag{5.3}$$

is formed for each point t in the image. A clustering algorithm is then used to perform the segmentation in the N-dimensional feature space.

Because Gaussian decomposition is not orthogonal, some researchers have also investigated the usage of wavelets frames models for texture segmenation[77]. The proposed method of this work also utilizes the multiresolution model and is similar to the wavelet packets approach in [26]. Yet two traits of the proposed method make it unique. First, the window size at every level of the MRA is an MxM segment, where M is an odd integer. This characteristic is significant when directional information is not of particular importance, as for example in cases where the texels lack orientation. Secondly, the decomposition is orthogonal, indicating conservation of the energy measure $\langle f, f \rangle$ $f \in V_j$ over subspaces embedded in $V_j$. Below two segmentation methods akin to the proposed DCT-based scheme are briefly reviewed.

### 5.2.1 Using Guassian Functions

The wide spread usage of Guassian elementary functions as window functions in texture analysis ([78]- [79]) is undoubtedly related to computational considerations and the fact that GEF's attain the lower bound for joint spatial/spatial-frequency resolution predicted by the *Uncertainty Principle*. Let $f \in L^2(R)$, $\triangle f$ its spatial variance and $\triangle \hat{f}$ the variance of $\hat{f}$, the Fourier transform of $f$. Then uncertainty principle says

$$\triangle_f \triangle_{hatf} \geq .5\pi \tag{5.4}$$

Gabor was among the first to suggest the use of GEFs as filters but it has long been known that for a GEF equally in (5.4) is attained. Later research into the receptive field profile of HVS suggests that joint space/spatial-frequency filtering (JSFF) plays a significant role in texture discrimination[80]. That being the case, methods based on JSFF have been adapted for artificial texture discrimination and GEFs have overwhelmingly become the filters of choice, particularly in structural models. A GEF may be tuned to any orientation and its spatial extent controlled.

In the context of image processing, a GEF is a 2D-Guassian modulated by a complex

sinusoid and is given by

$$F(x, y) = g(x', y')exp[2\pi\jmath(Ux + Vy)] \tag{5.5}$$

where

$$(x', y') = (x\,cos\theta + y\,sin\theta\,,\ -x\,sin\theta + y\,cos\theta) \tag{5.6}$$

for fixed real frequencies U and V to which F is tuned and g is given as

$$g(x, y) = \frac{1}{2\pi\delta_x\delta_y}\{-\frac{1}{2}[(\frac{x}{\delta_x})^2 + (\frac{y}{\delta_y})^2]\} \tag{5.7}$$

The spatial extent of F is controlled by $\delta_x$ and $\delta_y$ and the presence of the term $g(x', y')$ in 5.5 causes F to be rotated through an angle $\theta$ relative to the x-axis. It can be easily shown that

$$\hat{F}(u, v) = exp\{-\frac{1}{2}[(\delta_x[U - u]')^2 + (\delta_y[V - v]')^2\} \tag{5.8}$$

where $([U - u]'\,,\ [V - v]')$ is computed via an expression similar to 5.6. Clearly,$\hat{F}$ is a Guassian whose extent is under the control of $\delta_x$ and $\delta_y$, is rotated by $\theta$ relative to the u-axis and centered about the tuned frequency (U,V).

### 5.2.2 Using Wavelet Frames

The method of realizing texture segmentation using frames is a generalization of the filter bank approach [27][26]. However. in the case of frames the representation has built-in redundancies for an over-complete wavelet decomposition. A representation using frames can be realized using filters $H_\ell(\omega)$ and $G_\ell(\omega)$ defined in terms of the prototypes $H_0$ and $G_0$ as

$$H_0(z)H_0(z^{-1}) + H_0(-z)\,H_0(-z^{-1}) = 1 \tag{5.9}$$

$$G_0(z) = z\,H_0(-z^{-1}) \tag{5.10}$$

$$H_{\ell+1}(z) = H_0(z^{2^\ell})H_\ell(z) \tag{5.11}$$

$$G_{\ell+1}(z) = G_0(z^{2^\ell})H_\ell(z) \tag{5.12}$$

or equivalently

$$|H_\ell(\omega)|^2 + \sum_{j=1}^{\ell} |G_0(\omega)|^2 = 1 \tag{5.13}$$

where $\omega$ is defined as $exp(2j\pi)$. It is shown [77] that when 5.13 is satisfied the family of sequence $S = \{g_1(k-\ell), g_2(k-\ell), \ldots, g_N(k-\ell), h_N(k-\ell)\}$ is a tight frame for $\ell^2$. A fast discrete wavelet frame decomposition for $\ell^2(R^2)$ can be implemented using the block diagram similar ta a filter bank structure . The network outputs $d_{ih}, d_{id}$ and $d_{iv}$ represent the detail residual texture images at level respectively favoring the

horizontal, diagonal and vertical directions. Considering each output as a channel-filtered output, a feature vector $f = \{e_1, e_2, \ldots, e_N\}$ can be formed for

$$e_i = \frac{1}{|R_i|} \sum_{(\kappa,\ell)\in R_i} d_i^2(\kappa, \ell), \quad i = 0, 1, \cdots, N \tag{5.14}$$

where $e_i$ is the local variance of the output of the $i^{th}$ channel taken over a region $R_i$ and where $|R_i|$ is the number of points in $R_i$ and N the number channels.

### 5.2.3 DCT Texture Segmentation

Some texture segmentation algorithms proceed by processing the input image with specially designed filters which yield step like responses at texture boundaries, the goal being to reduce the computational burden as compared with algorithms which achieve segmentation on a pixel-by-pixel basis. This method is more suitable for supervisory segmentation where the possible texture classes are known a priori and the filters can be optimally designed. For robustness sake, the pixel-by-pixel method is adopted here and we continue to model the available texture image as $S_{J+1} \in L^2_\Omega(I^2)$ so that we can examine its projections on embedded subspaces . The energy distribution over these subspaces may then serve as a robust measure allowing for discrimination in the feature space. Let $S_{J+1}$ be an input texture image containing $K$ classes, $T_1, T_2, \ldots, T_K$, which can be uniquely represented in the feature space by

corresponding vectors $f_1, f_2, \ldots, f_K$. Each feature vector in this case is of the form

$$f_\ell = [E^\ell_{J+1}, E^\ell_J, \ldots, E^\ell_{J-N}] \tag{5.15}$$

where

$$E^\ell_J = [\mathbb{E}(V_J), \mathbb{E}(W_J), \mathbb{E}(W^1_J), \mathbb{E}(W^2_J)]_\ell, \ \ell = 0, \ldots, K. \tag{5.16}$$

$N$ is an integer depending on the number of layers in the MRA pyramid and $\mathbb{E}$ is the energy operator. Some researchers have advocated including the spatial coordinate of a pixel in its feature vector. The practice is not advantageous when the texture image contains homogeneous regions of large spatial extent.

The scheme used to classify each pixel is shown in figure 5.2.4. The transformation is performed using the fast DCT algorithms presented in chapter 4. Note that for each pixel the DCT-I is performed once, the projections on all embedded subspaces $V_J, W_J, W^h_J, W^v_J$, being efficiently implemented via the decomposition algorithm in chapter 3. The energy of each projection is also computed in the transform domain. Referring to figure 5.2.4, a $(2^{J+1}+1) \times (2^{J+1}+1)$ segment is extracted and modeled as an element of $V_{J+1}$. However, to facilitate the computation of projection energies it is simpler to consider the Chebyshev series expansion

$$s = \frac{a_{00}[s]\mathcal{T}_{00}}{4} + \sum_{m=1}^{\infty}\{\frac{a_{0m}[s]\mathcal{T}_{0m}}{2} + \frac{a_{m0}[s]\mathcal{T}_{m0}}{2}\} + \sum_{m,n=1}^{\infty} a_{mn}\mathcal{T}_{mn}, \tag{5.17}$$

which yields an energy formula

$$\mathbb{E}(s) = \frac{a_{00}^2[s]}{16} + \sum_{m=1}^{\infty} \frac{a_{om}^2[s] + a_{mo}^2[s]}{8} + \sum_{m,n=1}^{\infty} \frac{a_{mn}^2[s]}{4} \tag{5.18}$$

Using (5.17) plus results from chapter 3 and assuming $s = s_{j+1} \in V_{j+1}$, the projections coefficients are given by

$$a_{mn}[P_{V_j}\, s_{j+1}] = 2^{(1-j)} \epsilon_{j,m,j,n} \frac{\hat{s}_{j+1}(m,n)}{AA_{j+1}(m,n)} \qquad 0 \le m,n \le 2^j \tag{5.19}$$

$$a_{mn}[P^d_{W_j}\, s_{j+1}] = 2^{(1-j)} \epsilon_{j+1,m,j+1,n} \frac{\hat{s}_{j+1}(m,n)}{BB_{j+1}(m,n)}$$

$$2^j + 1 \le m,n \le 2^{j+1} \tag{5.20}$$

$$a_{mn}[P_{W^h_j}\, s_{j+1}] = 2^{(1-j)} \epsilon_{j,m,j+1,n} \frac{\hat{s}_{j+1}(m,n)}{AB_{j+1}(m,n)}$$

$$0 \le m \le 2^j, \quad 2^j + 1 \le n \le 2^{j+1} \tag{5.21}$$

$$a_{mn}[P_{W^v_j} s_{j+1}] = 2^{(1-j)} \epsilon_{j+1,m,j,n} \frac{\hat{s}_{j+1}(m,n)}{BA_{j+1}(m,n)}$$

$$2^j + 1 \le m \le 2^{j+1}, \quad 0 \le n \le 2^j \tag{5.22}$$

The above equations give the Chebyshev series coefficients for projections on the subspaces embedded in $V_{j+1}$. To simplify future reference to these results let $s_j, g_j^d, g_j^h$ and $g_j^v$ denote the projections in the order presented above. For example, $g_j^d = P_{W_j^d}[s_{j+1}]$. We are now in the position to offer fast transform domain algorithms to compute the projection energies.

### 5.2.4 Computation of Projection Energies

In this section a DCT-domain energy computation algorithm is presented. All Multiplication and division are done pointwise. The parameter M is the number of MRA levels desired.

*INPUT(J,M,* $s_{J+1}$ *)*

*Compute* $\hat{s}_{J+1}$

$\mathbb{E}(s_{J+1})$

$\ell = 0$

*Image(m,n)* $= \hat{s}_{J+1}$

*While* $\ell \leq M$

$$S(m,n) = 0.25 \frac{Image[0:2^{J-\ell},0:2^{J-\ell}](m,n)}{AA_{J-\ell}(m,n)}$$

$$G^d(m,n) = 0.25 \frac{Image[2^{J-\ell}+1:2^{J+1-\ell},2^{J-\ell}+1:2^{J+1-\ell}](m,n)}{BB_{J-\ell}(m,n)}$$

$$G^h(m,n) = 0.25 \frac{Image[0:2^{J-\ell},2^{J-\ell}+1:2^{J+1-\ell}](m,n)}{AB_{J-\ell}(m,n)}$$

$$G^v(m,n) = 0.25 \frac{Image[2^{J-\ell}+1:2^{J+1-\ell},0:2^{J-\ell}](m,n)}{BA_{J-\ell}(m,n)}$$

*Using* (5.18) *and [5.19-5.22] compute*

$\mathbb{E}(s)$

$\mathbb{E}(g^d)$

$\mathbb{E}(g^h)$

$\mathbb{E}(g^v)$

$\ell = \ell + 1$

$Image(m, n) = S(m = 0 : 2^{J-\ell}, n = 0 : 2^{J-\ell})$

*endWhile*

$OUTPUT(\mathbb{E}(s_{J+1}), \mathbb{E}(P_{V_{J-\ell}} s_{J+1}, P_{W^d_{J-\ell}} s_{J+1},$

$P^h_{W_{J-\ell}} s_{J+1}, P^v_{W_{J-\ell}} s_{J+1}, \ell = 0, 1, \ldots, M)$

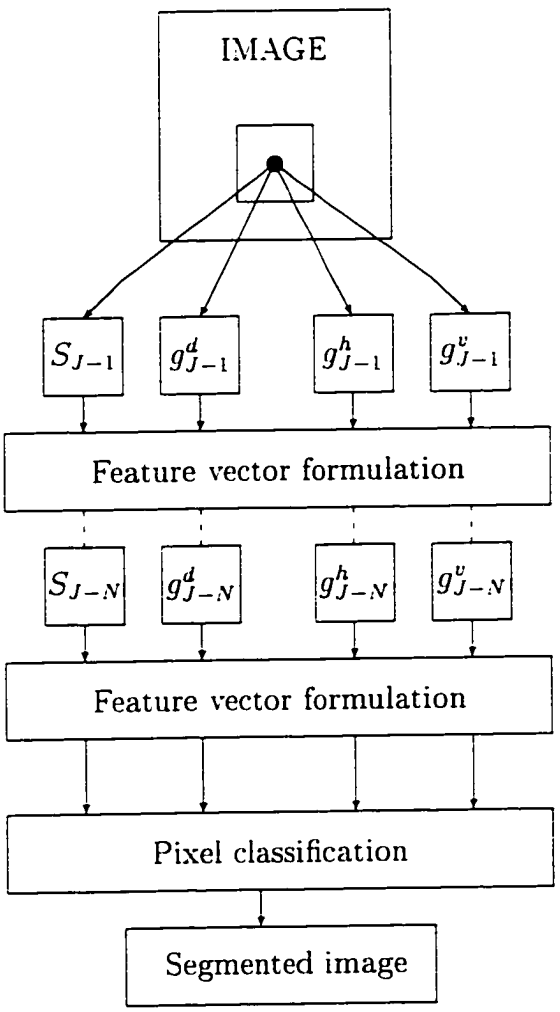


Figure 5.1: N-level GDCTWM-based texture segmentation block diagram. Pixels are classified using 17x17 block-size.

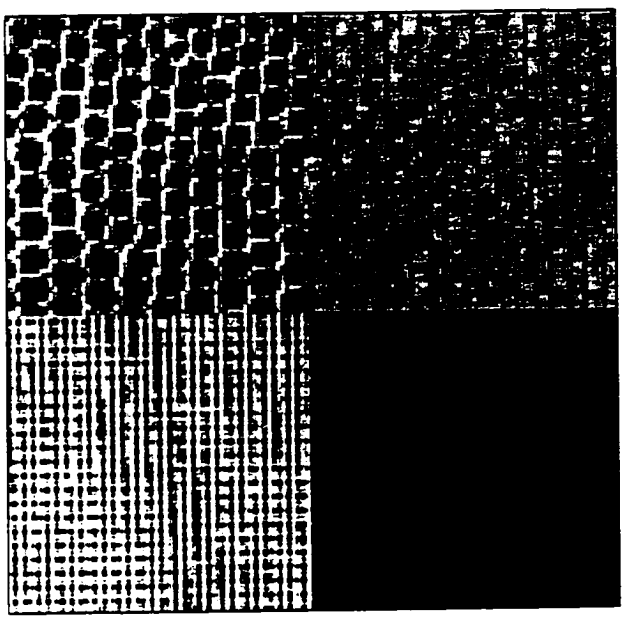

(a) texture image

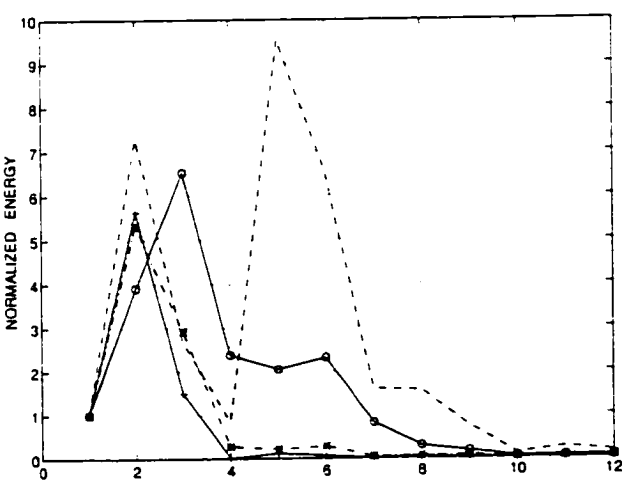


(b) feature vectors

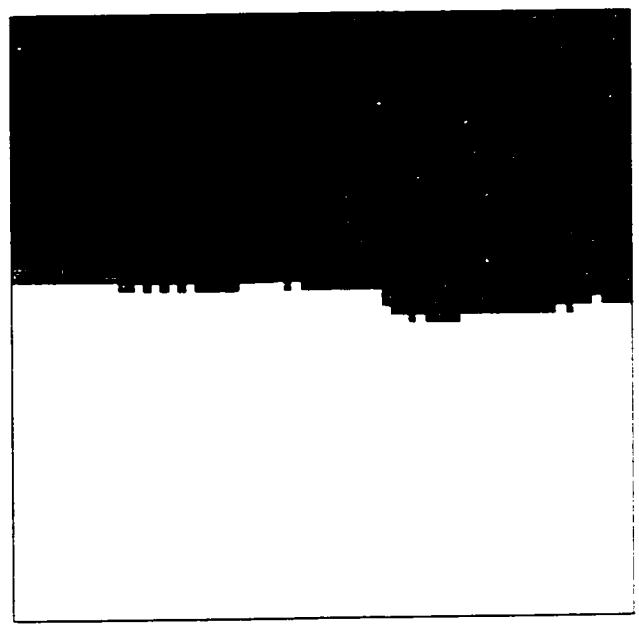

(c) segmented image

Figure 5.2: Segmentation of texture image shown in figure 4.7. (a) Original texture iamge (b) The feature vectors derived from normalized energy distribution. (c) The segmented image showing degraded boundaries due overlapping of extracted block segment used in classification analysis.

# Chapter 6

## Summary of Content

A DCT-based bidimensional orthonormal multiresolution analysis of $L^2_\omega(I)$ has been introduced. A novel image model for $S \in L^2_\omega(I)$ has also been proposed together with fast decomposition and reconstruction algorithms. The algorithms have been implemented using variants of the discrete cosine transform widely documented in available signal processing literature. More specifically, the separable two dimensional transforms employed have been derived from the DCT-I and DCT-II one dimensional transforms via tensor product extension method. Each of the four transforms utilize serves as the projection operator on an embedded subspace of $V_{j+1}$ where

$$V_{j+1} = V_j \oplus W_j^d \oplus W_j^h \oplus W_j^v$$

Suggested applications include data reduction, orthonormal image decomposition, and texture segmentation. It is well known that the KLT is optimal for data reduction and that the DCT is an asymptotic limiting case of KLT for the class of Markov-1 signals. Preliminary results using the MEPE measure of chapter 4 suggest that the DCT decomposition proposed in same chapter ought to perform favorably against wavelet subband decomposition in the area of data compression. The availability of fast DCT decomposition algorithms should in general make DCT image decomposition a competitive alternative to orthonormal subband schemes. The texture segmentation method of chapter 5 has been designed around feature vectors with energy components. Similar methods have been used by other researchers in the past. Computation of energy components has relied on first calculating the Chebyshev's coefficients of the projected signals. Explicit formulas for these coefficients have been shown to be readily available through an iterative algorithm involving a single DCT-I transform.

## 6.1 Future Research Objectives

Immediate future research goals include the following:

- To compare DCT and Subband methods for a range of applications and signal classes.
- To derive wavelet packets algorithms based on the wavelets descried in this dissertation.
- To investigate other possible signal models to be used with DCT decomposition methods

The first two objectives are clear. Currently the available signal S has been modeled as $S \in V_{j+1}$, depending on size. Theoretically, there is no requirement preventing an interpretation of the signal S as $S \in V_j$, $S \in W_j^d$, $S \in W_j^h$, or $S \in W_j^v$, subject to the constraint that the projections on three of the preceding subspaces are taken as zero. The third objective will include investigating the merits of such models.

# Bibliography

[1] S. G. Mallat, "Multiresolution Approximations and Wavelet Orthonormal Bases of $L^2(\Re)$," *Transactions of American Mathematical Society*, vol. 315, pp. 69–87, Sept. 1989.

[2] S. Mallat and S. Zhang, "Characterization of Signals from Multiscale Edges," *IEEE Transactions on Pattern Analysis Machine Intelligence*, vol. 14, pp. 710–732, July 1992.

[3] J. Daugman, "Two Dimensional Spectral Analysis of Cortical Receptive Field Profiles," *Vision Research*, vol. 20, pp. 847 -856, 1980.

[4] J. Daugman, "Uncertainty Relation for Resolution in Space, Spatial Frequency, and Orientaion Optimized by Two-Dimensional Visual Cortical Filters," *Journal of the Optical Society of America*, vol. 2, no. 7, pp. 1160 -1169, 1985.

[5] M. Porat and Y. Zeevi, "The Generalized Gabor Scheme of Image Representation in Biological and Machine Vision," *IEEE trans. PAMI*, vol. 10, no. 4, pp. 452–468, 1988.

[6] Marc Antonini et al., "Image Coding Using Wavelet Transform," *IEEE Transactions on Image Processing*, vol. 1, pp. 205–220, April 1992.

[7] R. A. Devore, B. Jawerth, and B. J. Lucier, "Image compression through wavelet transform coding," *IEEE Transactions on Information Theory, Special Issue on Wavelet Transform and Multiresolution Signal Analysis*, vol. 38, pp. 719–746, March 1992.

[8] P. D'Alessandro and R. Lancini, "Video coding scheme using DCT-pyramid vector quantization," *IEEE trans. Image Process.*, vol. 4, pp. 309–319, March 1995.

[9] O. Egger and W. Li, "Subband coding of images using asymmetrical filter banks," *IEEE trans. Image Process.*, vol. 4, pp. 478–485, April 1995.

[10] C. G. Zhou et al., "Mpeg video decoding with ultrasparc visual instruction set," *IEEE Digest of Papers COMPCON Spring*, pp. 470–475, March 1995.

[11] A. Averbuch, D. Lazar, and M. Israeli, "Image compression using wavelet transform and multiresolution decomposition," *IEEE trans. Image Process.*, vol. 5, pp. 4–15, Jan. 1996.

[12] E. A. B. da Silva and M. Ghanbari, "On the Performance of Linear Phase Wavelet Transforms in Low Bit-Rate Image Coding," *IEEE Transactions on Image Processing*, vol. 5, pp. 689–704, May 1997.

[13] R. L. de Queiroz and R. Eschbach, "Fast Downscaled Inverses for Images Compressed with M-channel Lapped Transforms," *IEEE Transactions on Image Processing*, vol. 6, pp. 794–807, June 1997.

[14] J. P. Leduc, J. M. Odobez, and C. Labit, "Adaptive Motion-Compensated Wavelet Filtering for Image Sequence Coding," *IEEE Transactions on Image Processing*, vol. 6, pp. 862–878, June 1997.

[15] R. Prost, Y. Ding, and A. Baskurt, "JPEG Dequantization Array for Regularized Decomposition," *IEEE Transactions on Image Processing*, vol. 6, pp. 883–887, June 1997.

[16] T. D. Tran and T. Q. Nguyen, "On M-channel Linear Phase FIR Filter Banks and Application in Image Compression," *IEEE Transactions on Image Processing*, vol. 45, pp. 2175–2184, September 1997.

[17] C. Bouman and B. Liu, "Multiple Resolution Segmentation of Textured Images," *IEEE Transactions on Pattern Analysis Machine Intelligence*, vol. 3, pp. 99–113, Feb. 1991.

[18] C. A.Bouman and M. Shapiro, "A Multiscale Random Field Model For Bayesian Image Segmentation," *IEEE Transactions on Image Processing*, vol. 3, pp. 162–175, Mar. 1994.

[19] R. Ting, R. Jeremiah, J. Barba, L. Habib, J. Kneuer, and J. Zhu, "The bandwidth and multiscale analysis of atm traffic," in *to appear in Proc. CSC/IEEE SPECS' 98*, (Reno, Nevada), July 19-22 1998.

[20] Xiong Zixiang and M. T. Orchard and Ya-Qin Zhang, "A Deblocking Algorithm for JPEG Compressed Images Using Overcomplete Wavelet Representations," *IEEE Transactions on Circuits and Systems for Video Technology*, vol. 7, pp. 433 – 437, April 1997.

[21] J. Zhang and J. W. Modestino, "A Model-fitting Approach to Cluster Validation with Application to Stochastic Model Based Image Segmentation," *IEEE Transactions on Pattern Analysis and Machine Intelligence*, vol. PAMI, pp. 1009–1017, October 1990.

[22] J. W. Modestino and J. Zhang, "A Markov Random Field Model-based Approach to Image Segmentation." *IEEE Transactions on Pattern Analysis Machine Intelligence*, vol. PAMI, pp. 606–615, June 1992.

[23] T. R. Reed and H. Wechsler, "Segmntation of Textured Images and Gestalt Organization Using Spatial/Spatial-frequency Representation." *IEEE Transactions on Pattern Analysis Machine Intelligence*, vol. 12, pp. 1–12, Jan. 1990.

[24] Nathalie Delprat et al. , "Asymptotic Wavelet and Gabor Analysis: Extraction of Instantaneous Frequencies." *IEEE Transactions Information Theory*, vol. 38, pp. 644–664, Mar. 1992.

[25] D. D. et al., "Texture Segmentation Using 2-D Gabor Elementary Functions." *IEEE Transactions on Pattern Analysis and Machine Intelligence*, vol. 16, pp. 130–149, Feb. 1994.

[26] A. Laine and J. Fan, "Texture Classification by Wavelet Packet Signature." *IEEE Transactions on Pattern Analysis Machine Intelligence*, vol. 15, pp. pp .1186 - 1197, Nov. 1993.

[27] T. Chang and C.C.Joy Kuo, "Texture Analysis and Classification with Tree-Structured Wavelet Transform," *IEEE Transactions on Image Processing*, vol. 2, pp. 429–441, Oct. 1993.

[28] F. W. Campbell and J. G. Robson, "Application of Fourier analysis to the visibility of gratings," *Journal of Physiology*, vol. 197, pp. 551–566, 1968.

[29] O. D. Faugeras, "Texture analysis and classification using a human visual model," in *Proceedings of International Conference on pattern Recognition*, (Tokoyo, Japan), pp. 549–552, 1978.

[30] M. Porat and Y. Zeevi, "Localized Texture Processing in Vision: Analysis and Synthesis in the Gaborian Space," *IEEE Transactions on Biological Engineering*, vol. 36, no. 1, pp. 115–129, 1989.

[31] M. Portnoff, "Time-Frequency Represenation of Digital Signals and Systems Based on Short-Time Fourier Analysis," *IEEE Transactions on Acoustic Speech, and Signal Processing*, vol. 28, no. 1, pp. 55–69, 1980.

[32] T. A. C. M. Classen and W. F. G. Mecklenbrauker, "The Wigner Distribution-a Tool for Time-Frequency Analysis: Part 2: Relations with Other Time-Frequency Signals Transformations," *Phillips J. Res.*, vol. 35, no. 6, pp. 372–386, 1980.

[33] L. T. Stanković, "Highly Concentrated Time-Frequency Distributions: Pseudo Quantum Signal Representation," *IEEE Transactions on Image Processing*, vol. 45, pp. 533–542, March 1997.

[34] L. Cohen, "Time-Frequency Distributions: a Review," *Proceedings of IEEE*, vol. 77, no. 7, pp. 941–981, 1989.

[35] D. L. Jones and T. W. Parks, "A Resolution Comparison of Several Time Frequency Representations," *IEEE Transactions on Signal Processing*, vol. 40, no. 2, pp. 413–420, 1992.

[36] R. Tolimieri and S. Winograd, "Computing the Ambiguity Surface," *IEEE Transactions on Acoustic Speech, and Signal Processing*, vol. 33, no. 4, pp. 1239–1245, 1985.

[37] R. Jeremiah, R. Ting, and J. Barba, "A bidimensional multiresolution analysis without edge effects.," *Submitted to IEEE Trans. on Image Processing.*

[38] R. Jeremiah, R. Ting, and J. Barba, "A generalized dctwm model," *Submitted to IEEE Trans. on Circiut and Systems for Video Technology.*

[39] H. Murakami, "Implementation and Perfect Reconstruction of a Maximally Decimated FIR Filter Bank Using Parallel Module Decomposition," *IEEE Transactions on Signal Processing*, vol. 45, pp. 328–332, Febuary 1997.

[40] T. Chen, "Nonuniform multirate filter bank: Analysis and design with $\mathcal{H}_\infty$ performance measure," *IEEE Transactions on Signal Processing*, vol. 45, pp. 572–582, March 1997.

[41] G. Karlsson and M. Vetterli, "Extension of finite length signals for sub-band coding," *Signal Processing*, vol. 17, pp. 161–168, 1989.

[42] Y. Meyer, "Ondelettes due l'intervalle," *Rev. Mat. Iberoamericana*, vol. 7, pp. 115–133, 1991.

[43] T. Kilgore and J. Prestin, "Polynomial wavelets on the interval," *Preprint . University of Rostock.*, 1994.

[44] A. Cohen and I. Daubechies, "A stability criterion for biorthogonal wavelet bases and their related subband coding scheme," ***Duke Mathematics Journal.*** vol. 68, pp. 313–335, 1992.

[45] V. E. Neagoe, "Chebyshev nonuniform sampling cascaded with the discrete cosine transform," *IEEE Transactions on Acoustic Speech, and Signal Processing.* vol. 38, pp. 1812–1815, 1990.

[46] G.Baszenski and M. Tasche, "Fast DCT-Algorithm, Interpolating Wavelets, and Hierarchical Bases," in *Wavelets, Images, and Surface Fitting* (A. L. M. P. Laurent and L. L. Schumaker, eds.), pp. 37–50, Wellesley, Massacchusetts: A K Peters, 1994.

[47] Z. Wang, G. A. Jullien, and W. C. Miller, "On Computing Chebyshev optimal nonuniform interpolation," *Signal Processing*, vol. 51, pp. 223–228, December 1996.

[48] R. L. Joshi and H. J. .et al, "Comparison of Different Methods of Classification in Subband Coding Schemes," *IEEE trans. Image Processing*, vol. 6, pp. 1473–1486, November 1997.

[49] K. A. Birney and T. R. Fisher, "On the modelling of DCT and subband image data for compression," *IEEE Transactions on Image Processing*, vol. 4, pp. 186–193, Febuary 1995.

[50] W. C. Chung and M. J. T. Smith, "Spatially-varying IIR filter banks for image coding," in *Proceedings of the IEEE International Conference on Acoustics, Speech and Signal processing*, vol. 5, pp. 570–573, April 1993.

[51] P. Sriram and M. W. Marcellin, "Image coding using wavelet transforms and entropy-constrained trellis-coded quantization," *IEEE Transactions on Image Processing*, vol. 4, pp. 725–733, June 1995.

[52] B. S. Chen, C. W. Lin, and Y. L. Chen, "Optimal signal reconstruction in noisy filter bank systems: Multirate Kalman synthesis filtering approach," *IEEE Transactions on Signal Processing*, vol. 43, pp. 2496–2504, November 1995.

[53] Z. Cvetković and M. Vetterli, "Discrete-time Wavelet Extrema Representation: Design and Consistent Reconstruction," *IEEE Transactions on Signal Processing*, vol. 43, pp. 681–693, March 1995.

[54] I. Daubechies, "Orthonornal Bases of Compactly Supported Wavelets," *Communication in Pure Applied. Mathematics*, vol. XLI, no. 41, pp. 909–996, 1988.

[55] I. Daubechies, A. Cohen, and J. Feauveau, "Biorthogonal Bases of Compactly Supported Wavelets," *Communication in Pure Applied Mathematics*, vol. XLV, no. 41, pp. 485–560, 1992.

[56] Ronald R. Coifman and Yves Meyer, "Orthonormal Wave Packet Bases," preprint, Yale University , New Haven, 1990.

[57] A. K. Soman, P. P. Vaidyanathan, and T. Q. Nguyen, "Linear Phase Paraunitary Filter Banks: Theory, Factorizations and Design," *IEEE Transactions on Signal Processing*, vol. 41, pp. 3480–3496, Dec. 1993.

[58] R. A. Gopinath and C. S. Burrus, "On Cosine-Modulated Wavelet Orthonormal Bases," *IEEE Transactions on Image Processing*, vol. 4, pp. 162–175, Feb. 1995.

[59] M. Vertelli and C. Herley, "Wavelets and Filter Banks: Theory and Design," *IEEE Transactionson on Signal Processing*, vol. 40, pp. 2207–2232, Sept. 1992.

[60] X.-G. Xia and B. W. Suter, "On the construction of two dimensional spatial varying FIR filter banks with perfect construction," in *Approximation Theory, Wavelets and Applications* (S. P. Singh, ed.), pp. 533–542, Netherlands: Kluwer Academic Publishers, 1995.

[61] I. Daubechies, *Ten Lectures on Wavelets*. Philadelphia: Siam, 1992.

[62] P. P. Vaidyanathan, *Multirate System and Filter Banks*. New Jersey: PTR Prentice Hall, 1993.

[63] Mark J. Smith and Steven L. Eddins, "Analysis/synthesis techniques for subband image coding," *IEEE Transactions on Acoustics Speech and Signal Processing*, vol. 38, pp. 1446–1456, August 1990.

[64] M. Haque, "A two-dimensional fast cosine transform," *IEEE trans. Acoust., Speech and Signal Process.*, vol. ASSP-33, pp. 1532–1538, Dec. 1985.

[65] N. Ahmed, T. Natarajan, and K. Rao, "Discrete cosine transform," *IEEE Transactions on Computers*, vol. C-23, pp. 90–93, Jan. 1974.

[66] M. Hamidi and J. Pearl, "Comparison of cosine and fourier transform of markov-1 signals," *IEEE Transactions on Acoustic Speech, and Signal Processing*, vol. ASSP-24, pp. 428–429, Oct. 1976.

[67] Y.-T. Chang, C.-L. Wang, and C.-H. Chang, "A new systolic architecture for fast dct transform," in *Circuits and Systems Connecting the World Proceedings-IEEE International Symposium on Circuits and Systems.*, vol. 2, (Atlanta, GA, USA.), pp. 485–488, 1996. Proceedings of the 1996 IEEE International Symposium on Circuits and Systems, ISCAS.

[68] M. T. Sun, T. C. Chen, and A. M. Gottlied, "VLSI implementation of 16x16 discrete cosine transform," *IEEE Transactions on Circuits and Systems*, vol. CAS-36, pp. 610–617, April 1989.

[69] C. Y. Hsu and H. D. Wu, "A new architecture for hardware implementation of a 16 x 16 discrete cosine ransform," *International Journal Electronics*, vol. 72, no. 4, pp. 593–603, 1992.

[70] H. Kitajima, "A symmetric cosine transform," *IEEE Transactions on Computers*, vol. C-29, pp. 317–323, April 1980.

[71] N. Ahmed and M. Flickner, "Some considerations of the discrete cosine transform," $16^{th}$ *Asilomar Conference on Circuits, Systems and Computers, Pacific Grove, CA*, pp. 295–299, Nov. 8-10 1982.

[72] H. Kitajima, "Energy packing efficientcy of the Hadamard transform," *IEEE Transactions on Communication*, pp. 1256–1258, Nov. 1976.

[73] L. Davisson, "Rate distortion theory and application." *Proc. IEEE*, vol. 60, pp. 800–808, July 1972.

[74] H. Derin and H. Elliott, "Modeling and Segmentation of Noisy and Textured Images Using gibbs Random Fields." *IEEE Transactions on Pattern Analysis Machine Intelligence*, vol. PAMI-9, pp. 39–55, January 1987.

[75] S. Geman and D. Geman, "Stochastic Relaxation, Gibbs distributions and the Bayesian Restoration of Images," *IEEE Transactions on Pattern Analysis Machine Intelligence*, vol. 6, pp. 721–741, November 1984.

[76] A. Speis and G. Healey, "Feature Extraction for Texture Discrimaination via Random Field Models with Random Spatial Interaction," *IEEE Transactions on Image Processing*, vol. 5, pp. 635–646, April 1996.

[77] M. Unser, "Texture classification and segmentation using wavelet frames," *IEEE Transactions on Image Processing*, vol. 4, pp. 1549–1560, November 1995.

[78] D. Gabor, "Theory of Communication," *Journal of the Institute Electrical Engineering*, vol. 93, no. 3, pp. 429–457, 1946.

[79] S. Qian and K. Chen, "Signal Representation Using Adaptive Normalized Guassian Functions," *Signal Processing*, vol. 36, pp. 1–11, 1994. Elsevier Publishers.

[80] S. Marcelja, "Mathematical description of the responses of simple cortical cells," *Journal of the Optical Society of America*, vol. 70, pp. 1297–1300, November 1980.

# IMAGE EVALUATION TEST TARGET (QA-3)

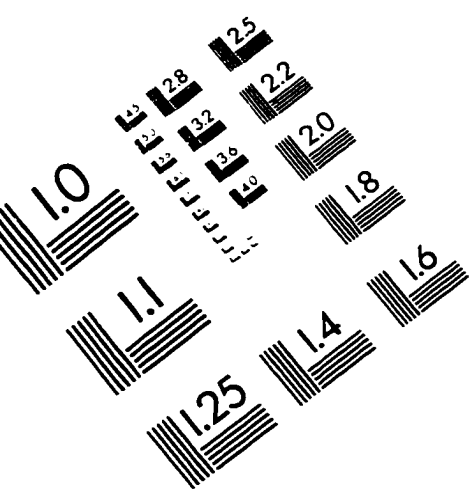


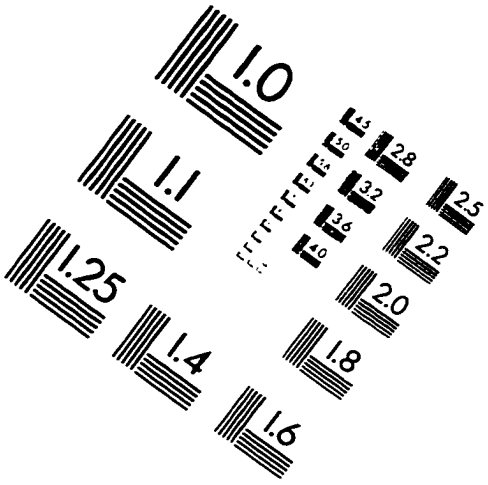


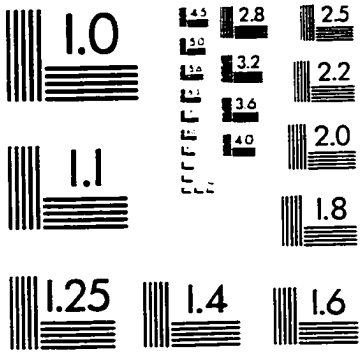


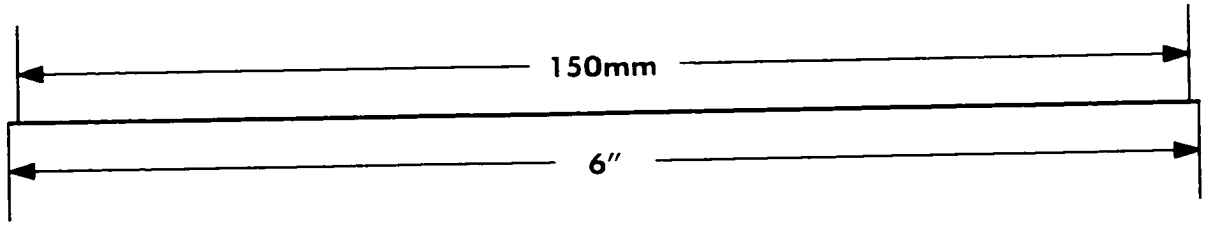


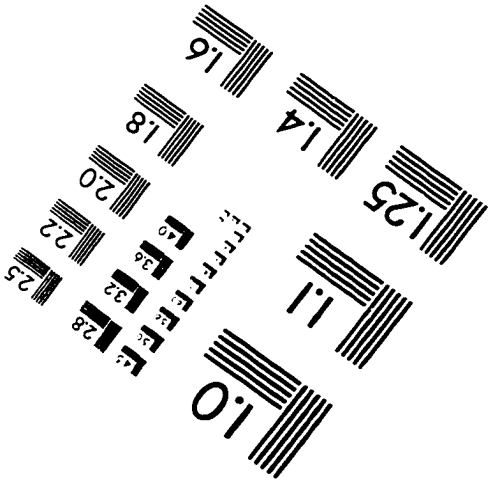


APPLIED IMAGE, Inc
1653 East Main Street
Rochester, NY 14609 USA
Phone: 716/482-0300
Fax: 716/288-5989